



Title	Metamorphism of stratified firn at Dome Fuji, Antarctica : A mechanism for local insolation modulation of gas transport conditions during bubble close off
Author(s)	Fujita, Shuji; Okuyama, Junichi; Hori, Akira; Hondoh, Takeo
Citation	Journal of Geophysical Research : Earth Surface, 114, F03023 https://doi.org/10.1029/2008JF001143
Issue Date	2009-09-30
Doc URL	http://hdl.handle.net/2115/39568
Rights	An edited version of this paper was published by AGU. Copyright 2009 American Geophysical Union.
Type	article (author version)
File Information	JGRES114-F03023.pdf



[Instructions for use](#)

Metamorphism of stratified firn at Dome Fuji, Antarctica: A mechanism for local insolation modulation of gas transport conditions during bubble close-off

Shuji Fujita ¹, Junichi Okuyama ^{2,3}, Akira Hori ^{2,4}, Takeo Hondoh ²

¹ National Institute of Polar Research, Research Organization of Information and Systems, Kaga, 1-9-10, Itabashi-ku, Tokyo, 173-8515, JAPAN

Tel.: +81-3-3962-5517; fax: +81-3-3962-5719 (sfujita@nipr.ac.jp)

² Institute of Low Temperature Science, Hokkaido University, N19, W8, Kita-ku, Sapporo, 060-0819, JAPAN

³ Present address: Advanced Applied Science Department, Research Laboratory, IHI Co., Ltd., Shin-Nakahara-Cho, 1, Isogo-ku, Yokohama, 235-8501, JAPAN

⁴ Present address: Department of Civil Engineering, Kitami Institute of Technology, 165 Koen-cho, Kitami, Hokkaido, 090-8507, JAPAN

Abstract

The evolution of the structure of a 112.59-m-long firn core recovered at Dome Fuji, East Antarctica, was investigated in order to improve understanding of firn densification and bubble formation processes, which are important for interpreting local insolation proxies used for astronomical dating of deep ice cores. Using selected samples, we measured physical properties including: (i) the relative dielectric permittivities in both the vertical and horizontal planes, (ii) the bulk density at a resolution of millimeters, (iii) the three-dimensional geometric structure of pore space, and (iv) crystal orientation fabrics. We found that the firn at Dome Fuji contains horizontal strata with thicknesses of several centimeters. Near the surface of the ice sheet, these strata are characterized by contrasting bulk density. Earlier field studies suggest that summer insolation causes densification of surface firn. Down to ~ 30 m, density maxima exhibited a clear positive correlation with the strength of structural anisotropy and c-axis clustering around the vertical. In contrast, the correlation is negative in deeper firn, confirming previous findings that initially less-dense firn became denser than initially dense firn. In addition, numerous examples of textures indicating that deformation preferentially occurred in weaker layers were found. Moreover, the initially dense firn layers were more permeable for air near the bottom of firn. We propose a model linking firn properties with conditions

for the gas transport processes near the bottom of firn. The model explains how stronger insolation can lead to bulk ice with a lower O_2/N_2 ratio and smaller total gas content.

1. Introduction

Deep ice cores from polar ice sheets preserve proxies of past climatic changes [e.g., *EPICA community members*, 2004; *Kawamura et al.*, 2007; *Petit et al.*, 1999; *Watanabe et al.*, 2003]. Deep ice originates from surface deposition of snow and frost, which undergo densification associated with mechanisms such as structural re-arrangement of grains, pressure sintering and plastic deformation in the firm of ice sheets [e.g., *Alley*, 1988; *Hondoh*, 2000; *Maeno and Ebinuma*, 1983; *Paterson*, 1994]. Thus, better understanding of these processes is important for ice core studies. In addition, better interpretation of paleoclimate proxy signals requires accurate dating of deep ice cores.

During bubble close-off near the bottom of the firm, firm air is progressively enriched with relatively small atoms and molecules such as He, Ne, O₂, and Ar relative to N₂ with time (and depth), whereas larger gases such as Kr, CH₄, CO₂ and Xe are not fractionated [*Huber et al.*, 2006; *Severinghaus and Battle*, 2006]. This size-dependent fractionation occurs in response to the preferential exclusion of small gases from shrinking bubbles to the residual firm air (open pores) by molecular diffusion through the ice lattice driven by pressure differences [*Huber et al.*, 2006; *Ikeda-Fukazawa et al.*, 2005; *Severinghaus and Battle*, 2006]. Fractionation of the O₂/N₂ ratio also occurs

between bubbles and clathrate hydrate crystals within the ice sheet [*Bender et al.*, 1995; *Ikeda-Fukazawa et al.*, 2001; *Ikeda et al.*, 1999] and between clathrate hydrate crystals and the atmosphere during the storage of ice cores after drilling [*Ikeda-Fukazawa et al.*, 2004; *Ikeda-Fukazawa et al.*, 2005]. *Bender* [2002] discovered that variations in the O₂/N₂ ratio of trapped gases occur cyclically, with ages between ca 160-385 ka in the Vostok (Figure 1) ice core. He found that these variations corresponded to changes in summer insolation at Vostok, suggesting that the O₂/N₂ ratio in trapped gases may provide an accurate astronomical timescale for very old ice cores. In explanation, he proposed that insolation affects snow metamorphism and grain properties in shallow firn, and that the insolation signature is retained throughout the firn, influencing O₂/N₂ fractionation during bubble close-off. *Kawamura et al.* [2007] found essentially the same relationship in the Dome Fuji (Figure 1) ice core for the previous ca 80-340 ka and accurately dated the O₂/N₂ records by validation with radiometric-dated time markers in the core. The O₂/N₂ records of the Dome Fuji and Vostok cores should be synchronous with local summer solstice insolation [*Kawamura et al.*, 2007]. However, the exact firn properties that affect close-off fractionation remain unknown [*Bender*, 2002; *Kawamura et al.*, 2007].

In addition, *Kawamura et al.* [2004] presented the total air content (TAC) from

the Dome Fuji ice core for the last 340 ka. They found that TAC was also synchronous with local summer solstice insolation: low TAC occurred at times of high summer insolation. They hypothesized that insolation modifies the strength of metamorphism within stratified firn, leading to modification of the gas diffusion paths near the base of the firn. *Raynaud et al.* [2007] investigated the TAC of the EPICA Dome C (Figure 1) ice core over the last 440 ka as a proxy for local insolation, proposing that long-term changes in TAC recorded in ice from the high Antarctic plateau were dominantly imprinted by local summer insolation. They hypothesized that more intense insolation caused grain growth near the surface, leading to decreased porosity at close-off.

Numerous studies have investigated firn densification processes and/or firn properties at various sites [e.g., *Alley*, 1988; *Anderson and Benson*, 1963; *Gow*, 1975; *Maeno and Ebinuma*, 1983; *Paterson*, 1994; *Rick and Albert*, 2005; *Courville et al.*, 2007]. Among these sites, both common and distinct processes have been found to be dependent on environmental conditions such as the accumulation rate, temperature and wind speed [e.g., *Alley*, 1988; *Paterson*, 1994]. The physical properties of a 112.59 m long core drilled in 1993 at Dome Fuji (see Figure 1, lat 77°19'S, long 39°40'E, 3810 m above sea level, annual accumulation rate of $\sim 27 \text{ kg m}^{-2}$ [*Kameda et al.*, 2008]), the second highest dome summit in East Antarctica, were investigated by *Watanabe et al.* [1997a], and

further in this paper. *Watanabe et al.* [1997a] conducted a preliminary investigation of the core including visual stratigraphy, bulk density, qualitative measure of permeability, grain size and air bubble volume. They reported that very developed depth hoar existed to a depth of ~6 m and that firm metamorphosed from depth hoar continued to ~40 m, maintaining the vertical structure characteristic of depth hoar. *Hondoh et al.* [1999] reported further physical properties of the core, including bubble volume during densification and bubble close-off.

The introduction of innovative measurement methods has provided new opportunities to better understand these physical properties. Using the physical principle of wave propagation in a birefringent medium, *Matsuoka et al.* [1998] demonstrated that the open resonator method can be used to measure the relative dielectric permittivity tensor and small microwave dielectric anisotropy of polycrystalline ice in ice core samples from Dome Fuji. In deep ice cores, crystal orientation fabrics (COF) have been observed to cause the difference in the dielectric permittivity between the vertical and the horizontal direction (hereafter we use the term dielectric anisotropy to denote the difference) [*Matsuoka et al.*, 1998]. However, firm is a dielectric mixture of ice and pore spaces, and it is well-known that ice grains and pore spaces develop vertically in snow and firm [e.g., *Alley*, 1987a; *Kojima*, 1967; *Pfeffer and Mrugala*, 2002]. This structural

anisotropy of pore spaces is also known to be associated with anisotropic dielectric properties [e.g., *Sihvola and Kong*, 1988]. For example, *Lytle and Jezek* [1994] observed that dielectric anisotropy in firn from a site near the summit of the Greenland ice sheet was 4-7 % of the relative permittivity due to the vertical elongation of snow grains. This value is markedly larger than that observed in the deep ice from Dome Fuji due to COF. This situation motivated us to assess the feasibility of using microwave dielectric anisotropy as a measure of the structural anisotropy of Dome Fuji firn.

In order to document the physical properties and their evolution in the Dome Fuji firn, several methods were employed and are discussed further in Section 2. Firstly, we improved the existing open resonator system [*Matsuoka et al.*, 1997; *Matsuoka et al.*, 1998] in order to obtain continuous measurements of the firn and ice cores. Secondly, continuous and high-resolution density measurements using the X-ray transmission method were performed [e.g., *Hori et al.*, 1999]. Thirdly, X-ray-absorption microtomography was used to determine the 3-D geometrical structure of ice grains and pore spaces [e.g., *Freitag et al.*, 2004]. Finally, X-ray pole figure measurements using X-ray diffraction methods were performed in order to obtain information on the COF. Published data on the qualitative measure of permeability, grain size [*Watanabe et al.*, 1997a] and air bubble volume [*Hondoh et al.*, 1999] in the firn at Dome Fuji were also

used in this study.

The dielectric anisotropy, geometrical structure, density, COF and the qualitative measure of permeability of the Dome Fuji firn were compared at millimeter and centimeter scales using selected samples from the 112.59 m long core [Watanabe *et al.*, 1997a]. The core was drilled in 1993 [Motoyama *et al.*, 1995] as a pilot hole for the deep ice core drilling conducted in 1994-1997 [Watanabe *et al.*, 1999]. The core was preserved at 223 K to prevent deterioration due to post-coring metamorphism until the measurements for the present study were completed in 2002 and 2003. Samples for the 2002/2003 measurements were from depths deeper than ~9.6 m, whose age is more than ~120 years before the coring in 1993 [Watanabe *et al.*, 1997b]. Preservation of the old (>~120 years) firn samples isothermally at ~223 K for ~10 years is almost equivalent to using a core sample from a deeper depth but by less than 1 meter; practically post-coring metamorphism cannot affect results of measurements presented in this study. The data collected in this study provide unprecedented information on evolution of firn metamorphism, suggesting a causal chain linking local insolation and conditions for gas transport in firn during bubble close-off.

2. Experimental methods

The methods used to obtain data from the ice core for this study are presented in Table 1 and described briefly below.

[Table 1]

2.1. Density measurement using X-ray transmission

The continuous density profile of the Dome Fuji shallow ice core measured using the X-ray transmission method have been previously reported by *Hori et al.* [1999]. The intensities of X-rays transmitted through an ice-core sample were continuously measured using an X-ray detector during translation of the sample across the X-ray beam. The X-ray intensity profile was converted into a density profile using a calibration curve for X-ray absorption based on ice thickness. The spatial resolution of the density profile was approximately 1 mm. Slab-shaped samples of dimensions given in Tables 1 and 2 were used for this study.

[Table 2]

2.2. Dielectric permittivity tensor measurement

An open resonator was designed for the Ka band (26.5-40 GHz) using the physical principle of wave propagation thorough a birefringent medium. Dielectric anisotropy was measured using an experimental procedure described previously [*Jones,*

1976; Matsuoka *et al.*, 1997; Matsuoka *et al.*, 1998]. This method enables precise measurement of the dielectric permittivity tensor and the dielectric anisotropy if appropriate sets of frequency and sample thickness are selected to reduce errors [e.g., Jones, 1976; Komiyama *et al.*, 1991]. Ten samples, a to j, were measured, and are described in Table 2. The depths were chosen so that sampling intervals along the core are roughly equally spaced, to see variation of the firm properties along depth. The resonator and the sample were placed in a cold room at a constant temperature of 258 K. The electrical field in the resonator has a Gaussian distribution with a half-power diameter of ~22 mm parallel to the slab and normal to the incident wave. The measured permittivity is thus a volume-weighted average within this Gaussian distribution. Source signals for the measurements were generated using a synthesized sweeper. Each sample slab was translated into the center of the electrical field by increments of five or ten millimeters. Permittivity components were measured in both the vertical and horizontal planes of the ice sheet (ϵ_v and ϵ_h , respectively). For all measurements, ϵ_v and ϵ_h were obtained simultaneously using a single frequency sweep without physical movement of the core [Jones, 1976; Matsuoka *et al.*, 1997; Matsuoka *et al.*, 1998]. In addition, only the real part (not the imaginary part) of the complex permittivity was measured. A resonant frequency of ~34 GHz was used. Accurate and precise values for the dielectric anisotropy $\Delta\epsilon (= |\epsilon -$

ϵ_h) were then calculated. Errors involved with the measurements are discussed below.

Each slab sample was prepared by cutting with a band saw followed by microtoming. The error associated with sample thickness was ± 0.2 mm, resulting in systematic errors in measured permittivity and $\Delta\epsilon$ of approximately ± 0.02 and ± 0.002 , respectively. The accidental errors in $\Delta\epsilon$ within a sample with single thickness were at most ± 0.001 . Thus, any variations of $\Delta\epsilon$ larger than the accidental error 0.001 were considered significant although measurable minimum $\Delta\epsilon$ is 0.003. The errors in $\Delta\epsilon$ were markedly smaller than the permittivity errors due to the physical principle of measurement [Matsuoka *et al.*, 1997]. The results and associated statistics obtained for ten samples used in the present study are given in Table 2.

2.3. Geometrical structure using X-ray absorption microtomography

A cylindrical specimen (15 mm in diameter x 15 mm in thickness), cut parallel to the core axis, was mounted on a rotating table positioned between a micro-focus X-ray tube (40 kV \times 50 μ A) and an X-ray intensifier (Shimadzu SMX-225CTS). The temperature of the specimens was maintained below 223 K with N₂ gas. Upon X-ray exposure, the intensifier captured fluoroscopic images from every angle of rotation about the vertical core axis. These two-dimensional (2-D) images were electronically captured

perpendicular to the core axis at 0.025-mm vertical intervals. A 3-D image with dimensions 512, 512 and 400 pixels for the x, y and z directions, respectively, was reconstructed. The 3-D image was cylindrical with a diameter of 13.5 mm and a height of 10 mm. A total of 23 specimens were measured, all sampled within the depth range of the ten samples listed in Table 2. An adjacent portion of the sample was used for the dielectric permittivity measurements so that dielectric permittivity and the geometrical structure data could be compared for all specimens.

2.4. Pole figure measurements using X-ray diffraction

The “Pole Figure Measurement” using the X-ray diffraction method was used to measure volume-weighted COF [Wenk, 1985]. This method does not give the orientation of individual crystals, instead giving a volume-weighted orientation, which is useful for measuring the preferred orientation of the c-axes in polycrystalline samples composed of very small grains. An automatic four-circle diffractometer (*Rigaku* SLX-2000) equipped with an X-ray tube (Cu, 60 kV \times 100 mA) was used for all measurements. A seven mm-thick horizontal section fixed onto a glass plate was measured at 253 K. The area measured was $30 \times 60 \text{ mm}^2$ in the horizontal plane and the incident depth of X-rays was approximately 1 mm depending on density of the firm samples. Seventeen core samples

were measured and seven pairs of measurements were made from pairs with differing density at the same depth, in order to investigate contrasting COF.

2.5. Qualitative measure of permeability using an air-sucking system

A continuous profile of a qualitative measure of permeability was measured by *Watanabe et al.* [1997a] using an air-sucking system on the firn core [*Langway et al.*, 1993]. Permeability (with dimension of area) is a specific material property that relates flow velocity to pressure drop across a sample by Darcy's law [e.g., *Albert et al.*, 2000]. However, the air-sucking system measures air pressure within the air-intake tube pressed onto the surface of the specimen. Therefore, the qualitative measure of permeability is expressed as pressure (Torr), and 760 Torr and 0 Torr correspond to free air and the perfectly impermeable firn, respectively. The term QMP is used in this paper to clearly distinguish this qualitative measure from real permeability. We note that *Langway et al.* [1993] and *Watanabe et al.* [1997a] termed the QMP as permeability and impermeability, respectively. QMP represents some volume of firn around the air-intake tube, with a diameter of 12 mm, pressed onto the surface of the specimen. The measured QMP can include airflow from many directions below the surface of the specimen and from a larger volume than the size of the air-intake tube. However, firn in the very vicinity of the

air-intake is the most effective to measured values.

3. Results

3.1 Variations in ρ

The density, ρ , for each of the ten samples is shown in Figure 2 as both raw data and as a volume-weighted average for comparison with the spatial resolution of the dielectric data (see below). Each sample showed large variations in ρ , with the right axis of Figure 3(i) showing the magnitude of variation as the standard deviation σ_ρ within each sample. Using all available detailed density data for the Dome Fuji cores, including both published and unpublished data by *Hori et al.*, [1999], 3-m-deep snow-pit measurements in 2004 (K. Fujita, personal communication) and a recent 4-m-deep snow-pit measurements in December 2007 (S. Fujita, unpublished data), σ_ρ was found to decrease gradually from a maximum of $\sim 40 \text{ kg m}^{-3}$ at the surface to a local minimum of $\sim 7 \text{ kg m}^{-3}$ at depth between ~ 40 and ~ 50 m. σ_ρ then increased to a local maximum of $10\text{-}20 \text{ kg m}^{-3}$ at ~ 65 m, then decreased gradually.

[Figures 2 and 3]

3.2 Variation of relative dielectric permittivity components with depth and density

The vertical and horizontal components of relative permittivity, ε_v and ε_h , as well as the difference between them, $\Delta\varepsilon$, were measured for each of the ten samples in Table 2. ε_v and ε_h were positively correlated with ρ for all samples (Figure 2), confirming that the dielectric permittivity is a function of firm density [e.g. Kovacs *et al.*, 1995]. The vertical component, ε_v , was larger than the horizontal component, ε_h , for all ten samples (Figure 2 (a)-(j)). ε_v was found to equal ε_h in samples (e) and (j) (see below), but no instances where $\varepsilon_v < \varepsilon_h$ were found. Several general trends in ε_v , ε_h , $\Delta\varepsilon$ and ρ were observed over the entire depth range (Figure 3(i) and (ii)): ε_v , ε_h and ρ tended to increase with increasing depth, while $\Delta\varepsilon$ generally decreased with increasing depth and exhibited marked fluctuations (Figures 2 and 3(ii) and Table 2). Also, $\Delta\varepsilon$ values in firm at depths to ~ 100 m were considerably larger than in deeper cores from 100-350 m where it was ~ 0.010 - 0.015 (Matsuoka *et al.* [1998] and unpublished data of S. Fujita). Within the individual samples, $\Delta\varepsilon$ was positively correlated with ρ in samples (a)-(d) (Figures 4 and 5), but tended to have negative correlation with ρ in deeper samples (e)-(j) (Figures 4 and 5). In samples (e) and (j), $\Delta\varepsilon$ was zero at certain depths.

The relationship between $\Delta\varepsilon$ and ρ at the scale of the sample length ($< \sim 0.5$ m) was different from the large-scale tendency (Figure 4 (dotted line) and Figure 5). The

shaded area in Figure 4 is the expected range within which $\Delta\epsilon$ can be explained by variability in COF [Azuma *et al.*, 2000], calculated using dielectric mixture theory in terms of ρ [Polder and Santen, 1946]. A realistic upper limit for polycrystalline pore-free polar ice near the surface at Dome Fuji was estimated to be 0.015 (Matsuoka *et al.* [1998] and unpublished $\Delta\epsilon$ data of the Dome Fuji deep ice core). In addition, the greater the pore-space within the firn (i.e., the lower ρ), the lower the effective value of $\Delta\epsilon$ due to COF. Figure 4 shows that COF variations may explain a part of $\Delta\epsilon$ only for the deepest samples, (i) and (j).

Vertical dotted lines in Figure 2 show pairs of small dips in $\Delta\epsilon$ and small bumps in ρ , suggesting the presence of physical processes linking anisotropy and density at the centimeter scale. These pairs appeared in samples (b) to (h), increasing from (f) to (h). In samples (i), near the bubble close-off depth, and (j), below the bubble close-off depth, few clear examples of these small dips in $\Delta\epsilon$ associated with bumps in ρ were observed.

[Figure 4 and 5]

3.3. Geometrical structure of firn

Figure 6 shows vertical and horizontal cross-sections of five firn samples selected from a total of 23 samples, obtained using X-ray absorption microtomography.

White and black areas indicate ice and pore-space, respectively, and whilst grain boundaries are not observable with this method, they should exist at the site of bonding [e.g., *Alley*, 1987a; *Arnaud et al.*, 1998]. The data provides the 3-D structure of firn and the progress of pore spaces towards bubble formation. Some of physical features of the five samples are listed in Table 3, and are explained below. The geometrical structure tended to vary with depth, with denser samples exhibiting relatively more bonding between ice portions. Several of the vertical images, (Figure 6, 1v and 2v), showed elongation in both ice and pore spaces in the vertical direction. However, no structural anisotropy was observed in the horizontal cross-sections. In sample 3, at a depth of 44.79 m where $\Delta\varepsilon$ was zero (Figure 2(e)), round shapes at the interfaces between ice and pore-spaces were not observed and both ice and pore-spaces appear fragmented, suggesting that a crushing event occurred in this layer (see Appendix). Another sample from 44.75 m depth exhibited similar morphology and interface characteristics (data not shown). In images of deeper firn (samples 4 and 5), ice occupied most of the area and the pores did not appear elongated. However, correlation-lengths in pore space [e.g., *Vallese and Kong*, 1981] both in the vertical direction (l_v) and in the horizontal direction (l_h) from the X-ray absorption microtomography revealed that the axial ratio (R_a), defined as l_v/l_h , were at least one or slightly larger for those samples (see Table 3 and below), indicating

that there was still slight structural anisotropy preserved at these depths. The correlation-lengths were calculated for the entire volume of the sample.

The applicability of $\Delta\varepsilon$ as an indicator of structural anisotropy [Lytle and Jezek, 1994] in the Dome Fuji firm was investigated (Figure 7). The axial ratio positively correlated with $\Delta\varepsilon$ for all samples with the exception of 44.75 m and 44.79 m where $\Delta\varepsilon$ was zero (discussed in Appendix), and thus demonstrates the relationship between $\Delta\varepsilon$ and structural anisotropy at Dome Fuji.

The volume of air bubbles isolated from the open channels of air was also examined. V_B is volume of isolated air bubbles within a unit weight of the firm sample. V_B values were averaged over 20 depths shallower than 69.74 m (Figure 7). The average V_B was $1.3 (2\sigma=1.0) \times 10^{-6} \text{ m}^3 \text{ kg}^{-1}$. The two samples, at 44.75-m and 44.79-m depth where $\Delta\varepsilon$ was zero, had V_B of 6.6 and $6.4 \times 10^{-6} \text{ m}^3 \text{ kg}^{-1}$, respectively. These unusually large values were excluded from the averaging. Causes of their extraordinary features are discussed in Appendix. At depths deeper than 69.74 m, V_B is much larger, up to $\sim 81 \times 10^{-6} \text{ m}^3 \text{ kg}^{-1}$, which is discussed in section 4.3.

[Table 3, Figure 6 and Figure 7]

3.4 Crystal orientation fabrics

The results of the volume-weighted COF measurements are shown in Figure 8. The results were first projected on an equal-area Schmidt net (data not shown). The c-axis distribution did not exhibit a strong azimuthal dependence. C-axes tended to cluster around the vertical or become inclined near the horizon depending on the sample. The c-axis clustering around the vertical was expressed using the median inclination angle (φ), a parameter used in previous studies [e.g., *Azuma et al.*, 2000]. φ is 0° , 60° , or 90° when the c-axes are completely aligned along the vertical, have a uniform distribution, or have a completely horizontal distribution, respectively. Although this method does not provide the orientation of the c-axis of each grain, φ can be estimated from the volume-weighted COF. φ was plotted versus density relative to the mean density of each sample ($\rho-[\rho_s]$) (Figure 8) to show dependency of COF on density within each sample. The values of φ ranged from $\sim 10^\circ$ to $\sim 80^\circ$. At depths shallower than 17.2 m, $\rho-[\rho_s]$ tended to be positively correlated with clusters of c-axes around the vertical, but this correlation tended to disappear or tended to be slightly negative for deeper samples (Figure 8).

[Figure 8]

3.5. Qualitative measure of permeability

A continuous profile of QMP was measured by *Watanabe et al.* [1997a], and it is

given in Figure 3(iii) and Figure 9. The depth zone below ~65 m is the transition zone where firn progressively becomes impermeable (Figure 3(iii) and Figure 9(i)). Figure 9(i) shows that QMP markedly decreases with increasing depth but with large (~200 Torr) fluctuations. Both the upper and lower limit of QMP are delineated.

[Figure 9]

4. Discussion

4.1. Summer insolation as the origin of layering near the surface

4.1.1. Two major components in the snow stratigraphy in the Dome Fuji region

The initial formation of the physical layering at Dome Fuji is discussed in order to better understand the evolution of porous structure, fabric and density at depths deeper than ~9.6 m. The initial formation of snow strata at and near the surface of the ice sheet has long been a topic of discussion [e.g., *Alley*, 1988; *Dang et al.*, 1997; *Li and Zwally*, 2004; *Paterson*, 1994; *Zhou et al.*, 2002]. On the plateau region around Dome Fuji, several pioneers [*Endo and Fujiwara*, 1973; *Koerner*, 1971; *Shiraiwa et al.*, 1996] described the characteristics of the snow cover over a wide region including Dome Fuji and the Plateau Station (Figure 1, lat 79° 15' S, long 40° 30' E, 3624 m above sea level). Based on a number of 1-m and deeper snow pits, both *Koerner* [1971] and *Shiraiwa et al.*

[1996] reported that the annual layering observed in snow stratigraphy had two components; one generally consisted of a thin (0.3-4.0 cm), hard, dense, fine-grained layer, often associated with a hoar layer and a bonded grain crust, while the other section was softer, less dense, coarse-grained, and more homogeneous. *Shiraiwa et al.* [1996] reported that the former was a solid-type depth hoar and the latter was a skeleton-type depth hoar. For convenience, these two types are termed in this study as the initially high-density firm (IHDF) and the initially low-density firm (ILDF), and these terms are used to specify the initial state of the layers at the surface even after they are modified by metamorphism. Both *Koerner* [1971] and *Shiraiwa et al.* [1996] reported that the IHDF formed in summer and the ILDF in winter. In particular, *Koerner* [1971] found that the IHDF formed when a drift of surface hoar formed from weak wind (wind velocity $> \sim 4$ ms⁻¹), based on thorough investigation on the effect of summer warmth and solar radiation through stratigraphic comparisons in early December and late January. He found that ice bridges formed between grains. *Fujita et al.* [2008] also found that the IHDF formed in a very short period of time near mid-summer through a comparison of snow type and density in the beginning of December 2007 and in the middle of January 2008 along a ~ 300 -km-long traverse route including Dome Fuji. They made numerous 20-cm-deep pits and found that hard and compacted snow appeared at the top few

centimeters of the ice sheet due to drifted hoar by weak wind (average wind velocity = $\sim 4.5 \text{ ms}^{-1}$), and the average snow density changed from $\sim 300 \text{ kg m}^{-3}$ to $\sim 370 \text{ kg m}^{-3}$ in the top three centimeters between the two sets of measurements. In addition, *Koerner* [1971] observed this annual alternation of firn types down to a depth of ten meters. These observations suggest that the IHDF is initially formed at the surface in summer and preserves its basic dense and hard condition to depths of ten meters.

4.1.2. Major causes of summer metamorphism

At Dome Fuji, the monthly rate of snow accumulation is approximately constant [*Kameda et al.*, 2008]. Monthly average wind speed does not vary markedly, being strongest in July (6.5 m s^{-1}) and weakest in January (4.5 m s^{-1}) [*Kameda et al.*, 2008]. Observations at Dome Fuji [e.g., *Azuma et al.*, 1997] have shown that the top several centimeters of the ice sheet are subjected to the strongest temperature gradient in summer due to annual and diurnal cycles in temperature. Thus, the ice sheet surface in summer is characterized by high temperature, intense insolation and strong temperature gradient in a rather moderate microclimate. Generally, these three factors have the strongest influence on snow metamorphism [e.g., *Colbeck*, 1989] and the snow-hardening process [e.g., *Ramseier and Sander*, 1966]) after deposition. *Gow and Ramseier* [1963] demonstrated

from South Pole data that sintering proceeded most rapidly at surfaces exposed to solar radiation and the atmosphere. The strong temperature gradient can cause strong vertical movement of vapor near the surface [e.g., *Alley et al.*, 1990; *Anderson and Benson*, 1963; *Paterson*, 1994; *Pfeffer and Mrugala*, 2002; *Zhou et al.*, 2002]. *Ramseier and Keeler* [1967] showed that evaporation and condensation are the most important processes in the sintering phenomenon. *Pfeffer and Mrugala* [2002] conducted a series of laboratory experiments in which they investigated how the temperature gradient and initial snow density control the type of depth hoar that forms within snow samples. They found that hard depth hoar develops when the initial density is higher. They observed that in solid-type depth hoar, grains were connected by necks with vertically preferred directions of grain elongation and organization of grain-to-grain chains. Their observations explain why the COF is often clustered around the vertical in firn, as earlier suggested by *Steffensen* [1966]. In addition, their study suggested that the IHDF remains distinct from the ILDF after decades of exposure to temperature gradients. Moreover, they demonstrated that the compressive strength of IHDF is correlated with the magnitude of the applied temperature gradient.

Overall, these earlier studies suggest that the annual alternation of firn types at Dome Fuji develop in response to summer insolation. We next discuss how the stratified

firn evolves with increasing depth.

4.2. Evolution of density, porous structure and fabric with depth in firn

4.2.1. Crossover of ρ and development of $\Delta\varepsilon$

The processes involved in the changes in ρ and $\Delta\varepsilon$ below 9.6 m to the bubble close-off depth are discussed. The fluctuation in ρ originated near the surface because σ_ρ is largest, $\sim 40 \text{ kg m}^{-3}$, within the shallowest two meters (Figure 3(i)). The σ_ρ of $\sim 40 \text{ kg m}^{-3}$ is comparable to the summer increase in surface density of $\sim 70 \text{ kg m}^{-3}$ which occurred at the top three centimeters at Dome Fuji in a summer [Fujita *et al.*, 2008]. Thus, the fluctuation in ρ is probably due to annual alternation of firn types initially formed and developed by summer insolation.

The correlations of ρ to $\Delta\varepsilon$ and also ε to $\Delta\varepsilon$ (Figures 4 and 5) change between ~ 40 m and ~ 60 m depth. The ρ - $\Delta\varepsilon$ and ε - $\Delta\varepsilon$ correlations must be similar because ε is a function of ρ [e.g. Kovacs *et al.*, 1995]. However, ρ was measured with one millimeter resolution whereas ε and $\Delta\varepsilon$ were measured simultaneously with a resolution of ~ 22 mm (Section 2 and Table 1). Thus, the sampling volumes are not the same for each even after volume-weighted averaging of ρ in order to adapt it to the resolution of ε and $\Delta\varepsilon$. Rather,

the $\varepsilon\text{-}\Delta\varepsilon$ correlations provide information complementing the $\rho\text{-}\Delta\varepsilon$ correlations under discussion. Similarly to the changes of the $\rho\text{-}\Delta\varepsilon$ correlations, the correlations of $(\rho\text{-}[\rho_s])$ to φ (Figure 8) change from positive to zero or slightly negative at depths between ~ 17 m and ~ 50 m. In addition, σ_ρ exhibited a local minimum at a depth between ~ 40 m and ~ 50 m (Figure 3(i)). Then the depth range between ~ 40 m and ~ 50 m is common for the changes of the $\rho\text{-}\Delta\varepsilon$ correlations and $\varepsilon\text{-}\Delta\varepsilon$ correlations (between ~ 40 m and ~ 60 m), $(\rho\text{-}[\rho_s])$ - φ correlations (between ~ 17 m and ~ 50 m) and the local minimum of σ_ρ (between ~ 40 m and ~ 50 m). Over a wide depth range from ~ 10 m to over 100 m, both ρ and $\Delta\varepsilon$ are expected to be monotonic, i.e., ρ should increase and $\Delta\varepsilon$ should decrease over time (depth) for a given firm layer. It is unlikely that φ evolves markedly within the firm, except for instances of crushing events such as those discussed in the Appendix. Therefore, it is highly unlikely that $\Delta\varepsilon$ and/or φ change greatly at depths between ~ 40 m and ~ 50 m to modify the $\rho\text{-}\Delta\varepsilon$, $\varepsilon\text{-}\Delta\varepsilon$ and $(\rho\text{-}[\rho_s])$ - φ correlations. The only realistic interpretation of this result would be crossover of ρ as proposed by previous studies [Freitag *et al.*, 2004; Gerland *et al.*, 1999], i.e., the initially less-dense firm layer becomes denser than the initially-denser firm layer, thereby creating local minimum in σ_ρ .

The IHDF is initially harder than the ILDF due to the apparent sintering phenomena as discussed in 4.1, i.e., grains in denser firm are bonded by ice bridges. The

IHDF also has higher structural anisotropy than the ILDF, indicating that structural anisotropy give additional compactive viscosity to the IHDF [Kojima, 1967; Pfeffer and Mrugala, 2002]. Thus, the ILDF deforms faster than the IHDF, which causes σ_p to be smaller with increasing time and depth.

An important factor in the initial densification of snow is the mainly structural re-arrangement of grains caused by the snow load [Alley, 1987b; Anderson and Benson, 1963]. Below a depth where closest-packing has already been attained, pressure sintering and dislocation creep become the dominant densification mechanisms [Maeno and Ebinuma, 1983]. However, these mechanisms should occur differently between the IHDF and ILDF because the consolidated states of these two types are very different and they should undergo different deformational histories. Initial densification proceeds more readily in the ILDF than in the IHDF because the ILDF is softer and has a greater capacity for packing, which makes it conducive to uniaxial compression. It is likely that the pressure sintering and dislocation creep occur more in the IHDF than in the ILDF from the initial stage because solid-type depth hoar is already hard and consolidated [Koerner, 1971]. The average ρ of the ILDF becomes equal to that of the IHDF at a depth between ~40 m and ~50 m where the density corresponds to approximately 630 kg m^{-3} (Figure 3(i)). This crossover is simply for density, and it does not imply changes in the

densification mechanisms at this depth. The grain size profile in Figure 3(iii) [Watanabe *et al.*, 1997a] shows that grain size tends to decrease to depths of ~65 m, implying that subdivision of old grains, polygonizations, dynamic recrystallization and production of new grains occur.

4.2.2. $\Delta\varepsilon$ as a marker to identify the origin of firm

At depths below ~30 m, the layers of firm cannot be identified as either from the IHDF or from the ILDF from ρ alone due to the crossover of ρ , instead $\Delta\varepsilon$ may be an important marker to identify the origin of the firm. The ILDF experiences more deformation and thus has a smaller value of $\Delta\varepsilon$, because deformation is destructive for the structural anisotropy; The IHDF experiences less deformation, leading to $\Delta\varepsilon$ values larger than in the ILDF. There are not distinct boundary $\Delta\varepsilon$ values between the IHDF and the ILDF because there should be a variety of intermediate states between them. Nevertheless, this $\Delta\varepsilon$ marker is useful and important in understanding the physical processes discussed below.

4.2.3. Densification below the crossover depth to the σ_p maximum

For depths greater than ~30 m, densification processes are associated with

slower shrinking of pore space (Figure 3(iv)). In addition, the value of $\Delta\varepsilon$ in samples (e)-(h) in Figure 4 is much larger than $\Delta\varepsilon$ limit explained from c-axis clustering, implying that both the ice matrix and pore space have vertically elongated shapes on average to depths of ~ 90 m. Grain size tended to increase after a minimum at ~ 65 m depth (Figure 3(iii), *Watanabe et al.*, [1997a]), implying that the normal grain growth process starts to dominate at this depth (Figure 3(iii)). σ_p increases after a minimum at depth between ~ 40 m and ~ 50 m to a maximum at ~ 65 m (Figure 3(i)), suggesting that the densification rate is larger in the ILDF than in the IHDF. The pairs of small dips in $\Delta\varepsilon$ associated with small bumps in ρ at centimeter scales (Figure 2) are interpreted to independently support the hypothesis that the ILDF tended to deform more readily than the IHDF, as $\Delta\varepsilon$ is smaller (dips in $\Delta\varepsilon$) due to the disruptions of the structural anisotropy associated with the enhanced densification (bumps in ρ). These pairs were most frequently found in samples (f), (g) and (h), suggesting that the preferential densification of the ILDF predominated over depths between ~ 54 m and ~ 88 m.

The ILDF tended to deform more readily than the IHDF due to stronger ice bonding between grains in the IHDF, as discussed in 4.2.1, and the higher structural anisotropy in the IHDF, giving it higher compactive viscosity [*Kojima*, 1967; *Pfeffer and Mrugala*, 2002]. In addition, the COF data in this study suggest that the IHDF is also

stronger in terms of the COF. The c-axes in the IHDF become clustered about the vertical axis (φ is 10-55°) and c-axes in the ILDF become distributed about the horizontal plane (φ is 70-80°) (Figure 8). According to the anisotropic flow law [Azuma, 1995], the strain rate for a given uniaxially compressive stress is highly dependent on φ : ice with φ close to 0° or 90° is hard, whereas ice with φ close to 45° is soft. The strain rate is determined by the position of maximum resolved shear stress for the basal plane of the ice crystal lattice. Models for COF development in response to uniaxial compression indicate that φ increases with increasing deformation due to the rotation of grains associated with dislocation glide on the basal plane [e.g., Azuma and Higashi, 1985; Azuma, 1994]. Under such conditions, the IHDF and ILDF tend to become harder and softer, respectively, when deformation is increased. Moreover, there is another possible factor that may affect mechanical properties of firn; high impurity content in snow deposited in winter was speculated to be the cause of the more rapid densification observed in the winter layers in Greenland [Freitag *et al.*, 2004]. Paterson [1991] hypothesized that high content of soluble ions such as chloride ions and sulfate ions might soften ice. In the Dome Fuji firn, sulfate ions show higher concentration in winter than summer [Iizuka *et al.*, 2004; Iizuka *et al.*, 2006]. Thus variations of sulfate ions are correlated to more rapid densification of the winter layer. However, it seems difficult to extract effects of sulfate

ions to mechanical properties; *Paterson's* hypothesis needs to be examined further. As for chloride ions, it is unlikely to be relevant because variation of the chloride ion is smoothed out in deeper firn at Dome Fuji [*Iizuka et al.*, 2006].

In summary, the ILDF is reasonably expected to deform more quickly than the IHDF due to these three major factors: initial consolidation due to sintering, structural anisotropy and the COF. The speculation for the impurity effect needs to be examined as well. Analysis of the depth- and time-evolution of these three mechanical properties of firn is an important topic for further development.

4.2.4. Densification below the σ_p maximum

At depths greater than the σ_p maximum at ~65 m, densification processes are associated with a progressive decrease of the qualitative measure of permeability (QMP, see section 4.3) due to shrinking pore space (Figure 3(iii) and 3(iv)). In addition, $\Delta\varepsilon$ progressively falls to the level explicable by c-axis clustering around the vertical in the samples (g)-(i) (Figure 4), implying that both the ice matrix and pore space have progressively lost their vertically-elongated shapes. σ_p does not vary significantly at depths below ~65 m (Figure 3(i)). In addition, the ρ - $\Delta\varepsilon$ correlations and the ε - $\Delta\varepsilon$ correlations are more negative in deeper samples (Figure 5), suggesting that the

deformation rate of the denser ILDF is as large as or larger than that of the less-dense IHDF. The pairs of small dips in $\Delta\varepsilon$ associated with small bumps in ρ at centimeter scales were not clear in samples (i) and (j) at depths greater than ~ 103 m, which are as deep as or deeper than the depth range of bubble close-off (Figure 2). The lack of clear pairs suggests that differences in density and structural anisotropy between the IHDF and the ILDF decrease once bubble close-off is completed. The densification of firm at depths below the σ_p maximum is related to air bubble formation processes and permeability within the firm (e.g., Figure 3(iii) and Figure 9), discussed further in section 4.3.

The values of $\Delta\varepsilon$ are less than 0.013 and 0.014 in samples (i) and (j), respectively (Table 2 and Figure 4), indicating that structural anisotropy of the pore space does not significantly contribute to the values of $\Delta\varepsilon$ at these depths (see Figure 7). These samples have negative ρ - $\Delta\varepsilon$ correlations (Figure 5). It is highly likely that the residual $\Delta\varepsilon$ are caused by the contrasting COF in the IHDF and the ILDF, i.e., the c-axes in the IHDF are more clustered around the vertical than the ILDF (Figure 8). The negative ρ - $\Delta\varepsilon$ correlation suggests that the ILDF is generally denser than the IHDF even at these depths and also during bubble close-off processes. At this stage of depth, the major cause of the contrasting densification seems to be COF, rather than ice bonding or the geometry of the pores. The impurity effect may be another possibility that needs to be examined in future.

4.3 Air bubble formation and permeability

Figure 9(ii) shows V_B in the core at depths deeper than ~ 78 m [Hondoh *et al.*, 1999]. V_B at the completion of bubble formation is $\sim 81 \times 10^{-6} \text{ m}^3 \text{ kg}^{-1}$. The data from the X-ray absorption microtomography show that micro-bubbles formed near the surface of the ice sheet [Lipenkov, 2000] comprise $1.6 (\pm 1.2)\%$ of V_B at the completion of bubble formation, and that normal bubbles, formed by the shrinkage of pore spaces [Lipenkov, 2000], appear mostly at depth below ~ 70 m. The bubble formation rate with reference to the final V_B at a depth z_c at the completion of bubble close-off is $\sim 5\%$, 10% , 25% , $\sim 50\%$ and $\sim 75\%$ at depths ~ 78 m, ~ 85 m, ~ 92 m, ~ 97 m and ~ 101 m, respectively. The starting depth (z_s) of bubble formation is defined as a depth where 5% of final V_B is attained. In case of Dome Fuji, z_s is ~ 78 m. We note that near the bottom of the firn there are two different phenomena: the bubble close-off, which is the depth at which all bubbles are closed, and the "lock-in depth" or "lock-in horizon", where air no longer mixes easily with the overlying firn air and the atmosphere [e.g., Battle *et al.*, 1996; Goujon *et al.*, 2003; Schwander *et al.*, 1997]. The latter horizon is often 3-8 m above the full bubble close-off in high accumulation sites. It has also been called the "air isolation depth". At Dome Fuji, it is possible that there is no major separation between the two horizons, as Kawamura *et*

al. [2006] did not find any evidence for a cessation of gravitational settling in the $\delta^{15}\text{N}$ data from firn air. The bubble close-off process is completed at $z_c \sim 104$ m, where the average density is $\sim 830 \text{ kg m}^{-3}$ (Figure 3(i) and Figure 9(ii)). z_c at a depth between 104 and 105 m was also independently determined in firn-air studies in the borehole at Dome Fuji [Ishijima *et al.*, 2007; Kawamura *et al.*, 2006; Sugawara *et al.*, 2003]. Bubble close-off was complete at depths where the upper limit of the QMP approached zero (Figure 9(i)). The firn is still permeable when the lower limit of the QMP approaches zero at ~ 98 m.

It is hypothesized that the higher and lower QMP values correspond to the IHDF and the ILDF, respectively. To verify this, the QMP profile was compared with $\Delta\varepsilon$ (Figure 2(g)-(i)). A positive correlation was found. In sample (h) in the middle of the bubble formation zone, the correlation was best and the correlation coefficient r was 0.45. The relation is statistically significant at $\% \alpha = 0.01$, indicating that the IHDF with structural anisotropy keeps the firn less dense and creates permeable layers in the bubble close-off zone. Figure 10 shows scatter plots of the QMP as a function of $\Delta\varepsilon$, ρ and ε , indicating the QMP is correlated to these. The correlation coefficients for samples (g) and (i) were lower at 0.40 and 0.37, statistically significant at $\% \alpha = 0.40$ and $\% \alpha = 0.20$, respectively. These statistically weak correlations are found within the very permeable firn (g) and near

close-off completion depth (i). Based on the correlation between the QMP and the origin of the firm in sample (h), we suggest that the numerous QMP peaks and troughs in Figure 9(i) also correlate with the IHDF and the ILDF layers, respectively. In contrast to the correlation between the QMP and $\Delta\varepsilon$, the correlations between the QMP and ρ were generally poor for the samples (g)-(i) (data are shown only for (h)). This implies that there is no critical density for pore close-off on the micro-scale and that pore close-off depends more on the history of a layer.

[Figure 10]

Although bubble close-off is attained only when the upper limit of the QMP approaches zero, processes within the ILDF during the bubble close-off process remain uncertain. If the ILDF is thick and the strata are horizontally extensive, the ILDF may constitute impermeable layers and effectively prevent any vertical interaction of air between the IHDF layers. A similar situation in which horizontally-extensive layers create a so-called “non-diffusive zone” on the order of several meters has been observed in the seasonal contrast between summer and winter accumulations at higher accumulation-rate sites [*Battle et al.*, 1996; *Kawamura et al.*, 2006; *Martinerie et al.*, 1992; *Schwander et al.*, 1993; *Schwander et al.*, 1997; *Severinghaus and Battle*, 2006].

However, based on comparisons of the QMP data of the slab-shaped firn core (Figure 9(i)) with the borehole-based firn air profiles at Dome Fuji [*Ishijima et al.*, 2007; *Kawamura et al.*, 2006; *Sugawara et al.*, 2003], we suggest that the upper limit of the QMP (a feature of the IHDF) are more important factors than the lower limit of the QMP (a feature of the ILDF) in controlling vertical gas exchange at low accumulation-rate sites. A non-diffusive zone at the deepest air sampling depth of 104 m was not observed at Dome Fuji. It indicates that, even when the lower limit of the QMP (lower dashed line) approaches zero at ~98 m depth where more than 50% of the bubble volume is already formed (Figure 9(ii)), the vertical diffusion of gas still occurs until the upper limit of the QMP fluctuation (upper dashed line) approaches zero below 104 m. The Vostok and Dome C sites also have very small non-diffusive zones (~2 m) [*Bender et al.*, 1994; *Landais et al.*, 2006], suggesting that the ILDF does not play a significant role in isolating layers at low accumulation-rate sites. Whilst the ILDF is impermeable, the permeable IHDF has vertical as well as horizontal connections. Such a situation is reasonable considering the irregularity of the depositional environment in the low accumulation area. *Koerner* [1971] and *Kameda et al.* [2008] showed that 8.5% and 8.6% of the area investigated had zero or negative surface mass balance over a year at Plateau Station and Dome Fuji, respectively. These numbers mean that there is a large proportion of area

where surface mass balance is smaller than the average and almost the same snow constitutes the top several centimeters of the ice-sheet surface for two consecutive years, becoming strongly imprinted by insolation. Temporal and spatial variability of surface mass balance should create a variety of thicknesses, hardness and depth of the IHDF and ILDF layers. The irregularity of the depositional environment in the low accumulation area creates a 3-D network of the IHDF and ILDF layers within the firn. Finally, vertical gas diffusion can be enabled by "gaps" or permeable spots in the ILDF. It is precisely these "gaps" that may play a critical role in allowing O₂ to escape to the atmosphere, and thus allow the bulk ice O₂/N₂ to fall below ambient.

4.4. A model for modulation of conditions for gas transport by local insolation in firn

4.4.1. An idealized model

A model forming a qualitative link between local insolation and the O₂/N₂ ratio of the trapped gas (and also TAC) in the ice core is proposed in the light of results discussed above. Figure 11 schematically outlines this model, described in detail below:

(i) The annual alternation of firn types develops in response to summer insolation. Therefore, the firn contains horizontal strata with thicknesses of several

centimeters. These were discussed in section 4.1. Summer insolation creates the IHDF layer of the surface firn. ILDF forms as winter layers that did not receive direct irradiation from summer insolation at the surface of the ice sheet.

(ii) The IHDF is initially harder than the ILDF due to ice bonding between grains, structural anisotropy and effect of COF. The difference in mechanical strength allows preferential deformation of weaker layers, causing the ILDF to become denser than the IHDF. The depth of the crossover in density is between ~ 40 and ~ 50 meters at present time at Dome Fuji. These results were discussed in section 4.2.

(iii) During the bubble close-off process from its starting depth ($z_s \sim 78$ m at present time at Dome Fuji) to its completion depth ($z_c \sim 104$ m), the ILDF continues to be denser than the IHDF by $\sim 10 \text{ kg m}^{-3}$ due to preferential deformation. Air bubbles in the ILDF tend to form earlier and at shallower depths than those in the IHDF. The IHDF layers tend to remain permeable to air for longer. In addition, the IHDF constitutes a 3-D network in the firn. The persistence of the IHDF determines the deepest limit of the vertical permeable firn in the bubble close-off zone. These results were discussed in section 4.3.

(iv) A pressure lag, Δp , occurs between the air in open pores and air in both closing and closed air bubbles. The internal pressure of an air bubble is equal to the

atmospheric pressure at the time of formation and gradually approaches the overburden pressure by compression in the firn [e.g., *Lipenkov, 2000; Ikeda-Fukazawa et al., 2001*]. Thus, the internal pressure of an air bubble depends on the time of its formation. For example, overburden pressures were estimated from the density profile in Figure 3(i) and they are higher than the atmospheric pressure by 0.45 MPa and 0.65 MPa at $z_s=78$ m and $z_c=104$ m, respectively. It has been presumed that the differences in pressure between closing/closed air bubbles and air in open pores drive two processes: effusion of air from closing bubbles to open pores through a small opening [*Bender, 2002*] and permeation of gas molecules from closed bubbles to open pores through the ice lattice [*Huber et al., 2006; Ikeda-Fukazawa et al., 2005; Severinghaus and Battle, 2006*]. The former process, Δp -driven effusion, was proposed by *Bender* [2002] as a mechanism for gas fractionation. However, we suggest that effusion is unlikely to fractionate, because the channel sizes should be much larger than molecular size and also are quite variable in size. Instead, we suggest that effusion decreases the close-off porosity and hence decreases TAC without fractionation of gas molecules. In contrast, the latter process, Δp -driven permeation of gas molecules, causes both fractionation of gas molecules and a decrease in the air content of bubbles. Size-dependent fractionation occurs due to the preferential exclusion of small gases from shrinking bubbles by molecular diffusion through the ice lattice [*Huber et al.,*

2006; Ikeda-Fukazawa *et al.*, 2005; Severinghaus and Battle, 2006]. Thus, both accumulation of O₂-enriched gas in the residual firn air and depletion of O₂/N₂ ratio in air bubbles occur in the bubble formation zone. TAC also decreases in the bubble formation zone.

(v) The O₂-enriched gas in the residual firn can escape to the ice sheet surface rapidly over a time scale of the order of 10¹ years due to the upward diffusive flux of enriched firn gas through channels of open pores [Severinghaus and Battle, 2006; Ishijima *et al.*, 2007; Kawamura *et al.*, 2006; Sugawara *et al.*, 2003] at a depth where the QMP peaks are preserved (Figure 9(i)). At both Vostok [Bender *et al.*, 1994] and Dome Fuji (K. Kawamura, personal communication, 2008), the O₂/N₂ ratio near the bottom of firn is higher than present atmosphere only by ~0.3 ‰, much smaller than at sites experiencing the lock-in effect (typically several ‰, e.g., Huber *et al.*, [2006]; Severinghaus and Battle, [2006]), suggesting that upward diffusive flux of O₂-enriched gas is sufficiently large to allow escape through the surface.

(vi) Strata composed of the two types of firn can act as a centimeter-scale macroscopic zone for the Δp -driven transport of gas molecules. The mechanical persistence of paths for the vertical diffusion of gas through open pores depends on the distinctness of the alternation in firn-type due to variations in intensity of insolation. For

example, the upper limit of QMP in Figure 9(i) should be higher (lower) for ages when summer insolation were more (less) intense and, physically, the firm is harder (softer) due to strength of ice bonding, geometry of pore spaces, the effect of COF and additional possible effects from impurity. These conditions are also schematically explained in Figure 11(i). The changes of the upper limit of QMP in Figure 9(i) means that the depth of bubble close-off, z_c , also changes since the gradient of QMP versus depth is determined by stress/strain-rate relations within each type of firm (Figure 11(i)). The changes in z_c further means that age of the firm, defined as the time of the completion of bubble close-off $t(z_c)$, also changes. Here, $\tau (t(z_c) - t(z_s))$ is defined as the duration from the start of bubble close-off in the ILDF until the completion of bubble close-off in the IHDF. τ is longer (shorter) when summer insolation is more (less) intense. Importantly, it is assumed that the depth of the start of bubble formation in the ILDF is not significantly affected by insolation because this layer did not receive direct irradiation. Therefore, the shallower part of the bubble formation rate is not significantly affected by insolation (schematically shown in Figure 11 (ii) and (iii)). In contrast, bubble formation in depths deeper than this should be retarded (Figure 11 (ii) and (iii)). The intensity of summer insolation affects τ and hence determines the total transport of gas molecules, assuming that the total amount of gas transport is approximately proportional to the product of τ and Δp . This principle

should work for both the permeation and the effusion mechanisms. In a closing air bubble, shrinkage is a time-dependent creep process of the ice matrix associated with surface diffusion and volume diffusion of water molecules [e.g., *Paterson, 1994*]. For a closed air bubble, permeation is a time-dependent transport process of the gas molecules within the ice matrix. Changes in the overburden pressure near the bottom of the firm may also affect the total amount of gas transport. In summary, modulation of τ and Δp are hypothesized to be the factors controlling the total amount of gas transport.

[Figure 11]

4.4.2. A preliminarily quantitative check

A preliminarily quantitative examination was attempted. In particular, the diffusion length of gas molecules through the ice lattice, typical change in τ and typical quantities of effusion and permeation are examined. Table 4 gives variable range of values related to the modulation of gas transport conditions by the local insolation at Dome Fuji for a period from 350 ka BP to present. Compatibility among the local insolation, O_2/N_2 ratio in trapped gases, TAC and variable range of depth for bubble formation are examined.

[Table 4]

(i) Diffusion length: *Ikeda-Fukazawa et al.*, [2004] and *Ikeda-Fukazawa et al.*, [2005] estimated the diffusion coefficients of O₂ and N₂ within an ice lattice based on molecular dynamics simulations. The diffusion coefficients of O₂ and N₂ within ice lattice are $1.6 \times 10^{-11} \text{ m}^2 \text{ s}^{-1}$ and $1.2 \times 10^{-11} \text{ m}^2 \text{ s}^{-1}$, respectively, at 216 K, at the average present temperature at Dome Fuji [*Kameda et al.*, 1997]. Also, the age of firn at depths of z_s (~78 m) and z_c (~104 m) are ~1.8 ka BP and ~2.5 ka BP, respectively [*Watanabe et al.*, 1997b], resulting in a time span τ of ~0.7 ka. Diffusion length L is defined as:

$$L = (D_n \cdot \tau)^{0.5} \quad (1)$$

where D_n is the diffusion coefficient of gas molecule n . Substituting in the D_n values for O₂ and N₂ gives L of 0.6 m and 0.5 m, respectively. These lengths of diffusion are much larger than the typical thickness of strata at low accumulation sites such as Dome Fuji, confirming that the permeation mechanism can actually occur at these thicknesses if there is a pressure lag, Δp .

(ii) Typical changes of τ . Variation in the range of local summer insolation due to astronomical precession cycles is assumed to be up to ~30% (Table 4). Such variation can

cause a change in the depth of the completion of close-off (Δz_c) by ~ 2 meters, considering the gradient of the upper limit of QMP versus z in Figure 9(i). The relationship between QMP and local summer insolation was approximated as linear. A Δz_c of ~ 2 m gives changes in τ of $\sim 8\%$ ($\Delta z_c / (z_c - z_s)$), given $z_s \sim 78$ m and $z_c \sim 104$ m. This is similar to the amplitude of the TAC cycles observed in the Dome Fuji ice core (Table 4) [Kawamura *et al.*, 2004]. This very rough quantitative estimation at least implies that the model has no serious disagreement with the measured variation in TAC.

(iii) Possible change of the gas transport due to the permeation mechanism: The range of the O_2/N_2 ratio due to astronomical precession cycles is assumed to vary by ~ 12 ‰ as observed in Dome Fuji ice core (Table 4) [Kawamura *et al.*, 2007]. We estimate the proportion of air that would have to escape from a given closed air bubble through the permeation mechanism to cause a change in the ratio by ~ 12 ‰. The flux of gas through the ice is assumed to be proportional to the permeation coefficient, which is the product of the diffusivity and solubility [Equation 3 in Severinghaus and Battle, 2006]:

$$j_n \approx D_n X_n \Delta p_n / x_w \quad (2)$$

where j_n is the flux of gas n per unit area, D_n is again the diffusivity of gas n in the ice lattice, X_n is the solubility, Δp_n is the partial pressure differences across the ice wall and x_w is distance through the ice wall. Assuming that differences in Δp_n are negligibly small for O_2 and N_2 and that x_w is common, equation 2 is simplified as:

$$j_n \propto D_n X_n \Delta p_n \quad (3)$$

The product of D_n and X_n gives the permeation coefficient. Again at 216 K, X_n of O_2 and N_2 within ice lattice are 2.3×10^{-10} and 1.4×10^{-10} mol m_{ice}⁻³ Pa⁻¹, respectively [Ikeda-Fukazawa *et al.*, 2005]. Then, the permeation coefficient $D_n X_n$ is 3.6×10^{-21} and 1.6×10^{-21} mol m_{ice}⁻¹ s⁻¹ Pa⁻¹, for O_2 and N_2 , respectively. Considering that the permeation coefficient of O_2 is larger than that of N_2 by a factor of 2.3, we estimate that for a given closed air bubble, the loss of ~3% air agrees with a change in the O_2/N_2 ratio of ~12 %.

Finally, we hypothesize that nearly half of the variation in range of the TAC (~7%) is due to the permeation mechanism (~3%) and that the residual (~4%) is due to gas loss by the effusion mechanism.

4.4.3. Comparison with earlier hypotheses

There have been several ideal models hypothesizing a link between local insolation and the O₂/N₂ ratio of the trapped gas and also the link between local insolation and TAC [e.g., *Bender*, 2002; *Severinghaus and Battle*, 2006; *Kawamura et al.*, 2004; *Raynaud et al.*, 2007; *Hutterli et al.*, 2008]. The model presented in this paper explains the O₂/N₂ ratio and TAC together, whilst earlier ideal models tended to discuss them independently. Earlier hypotheses are reviewed in the light of the new data and present discussion. Each mechanism is discussed below.

(i) Effusion mechanism during bubble close-off: *Bender* [2002] hypothesized that the cause of O₂/N₂ fractionation was gas effusion through air-channels during the pore closure. In the present model, effusion is interpreted as one of major mechanisms for loss of TAC but not as a cause of O₂/N₂ fractionation.

(ii) Permeation mechanisms: *Ikeda-Fukazawa et al.* [2005] developed a model of gas loss through molecular diffusion from clathrate hydrates within the ice-core through ice crystals toward the ice-core surface during a period of core storage. *Severinghaus and Battle* [2006] presumed that fractionation was caused by selective permeation of gas through the ice lattice from slightly overpressured bubbles. The present model extends these ideas, proposing that permeation arises from flow from

overpressured bubbles in the ILDF to channels of open pores in the IHDF. This stratified structure is efficient for the transport of gas.

(iii) Lock-in model to explain loss of TAC: *Kawamura et al.* [2004] hypothesized that insolation modifies the strength of metamorphism within stratified firn, leading to modification of gas diffusion paths near the base of the firn. They assumed that the summer layer could result in a sealing effect in the firn, forming a so-called lock-in zone near the close-off depth. Such a lock-in effect was not supported by the data in the present work. However, the local insolation modulation of the strength of metamorphism within stratified firn is the essential basis of the present model as in *Kawamura et al.*'s hypothesis. Also, this hypothesis may still be valid for explaining higher-accumulation sites such as Greenland, where O_2/N_2 has been shown to also vary inversely with insolation [e.g. *Suwa and Bender*, 2008]. At these sites there are indeed well-developed non-diffusive zones, in which O_2/N_2 is enriched.

(iv) Grain size effect: *Raynaud et al.* [2007] hypothesized that more intense insolation could cause grain growth near the surface, leading to decreased porosity at close-off. *Raynaud et al.*'s hypothesis is independent of the mechanisms discussed in the present model. In order to examine *Raynaud et al.*'s hypothesis, layering of grain size, porosity and QMP in the bubble formation zone would need to be investigated to find

correlations between grain size and other physical properties.

(v) Effect of pore shape: The vertically-elongated shape of pore spaces may play some role in the vertical diffusivity of gas thorough channels of open pores in the bubble close-off zone, explaining variations in the O₂/N₂ ratio and the TAC [e.g., *Hutterli et al.*, 2008]. However, we interpret that this is unlikely for two reasons. Firstly, the axial ratio becomes only as large as 1.0 in the bubble formation zone and firm with such isotropic pore spaces does not allow preferential diffusivity of air along the vertical. Considering the crossover of ρ , stronger diffusivity of air occurs due to the mechanical strength of the porous structure. Secondly, non-diffusive layers in the ILDF can cut the vertical diffusion of air from immediately neighboring IHDF layers through the sealing effect. This sealing effect can occur only locally, since the 3-D network of the IHDF allows vertical diffusion as discussed in section 4.3.

The present model is characterized by the local insolation modulation of mechanical properties in the IHDF; this was not considered in the earlier ideal models mentioned above. Mechanical properties of firm in terms of ice bonding between grains, geometrical shape of pore spaces, COF and additional possible effects from impurity are a subject that should be explored extensively.

4.4.4. Implication for other sites with higher accumulation rate

The present model was proposed based on the data from a low accumulation site of Dome Fuji. Applicability of the model for other sites with higher accumulation rate should be examined. The crossover of ρ occurs commonly at sites with higher accumulation rate such as Berkner Island [Gerland *et al.*, 1999] and Greenland [Freitag *et al.*, 2004]. The crossover seems to be universal behavior of firn under climatic conditions of these sites and Dome Fuji ranging from -25 °C and 200 mm/a to -55 °C and 30 mm/a in temperature and in annual accumulation rate, respectively. Thus, as far as stratification formation is linked to summer insolation, the model should work at high accumulation sites through the common crossover phenomenon. Higher accumulation rate may reduce exposure time of surface snow to direct effect of irradiation, decreasing degree of metamorphism within unit thickness. At the same time, unit layers comprising stratification may be thicker due to larger accumulation. Also, the shallowest impermeable layers linked to the ILDF forms the non-diffusive zone. Then, in the model, τ would be smaller due to shallower formation of the non-diffusive zone. In addition, air molecules need to be transported for longer distances from the ILDF to the IHDF due to thicker ILDF. These conditions can cause the magnitude of the local insolation modulation smaller. An example may be an observation that O₂/N₂ fractionation in the

GISP2 (accumulation >200 mm/a and nearly 10 times higher than at Dome Fuji) core is weaker than that in Vostok ice core by ~ 2 ‰ (Figure 6 in [Suwa and Bender, 2008]).

5. Concluding remarks

Several physical properties of firm including structural anisotropy, density and COF were measured at Dome Fuji in order to better understand densification and bubble formation processes. We found the alternation of firm types between IHDF and ILDF affect these physical properties throughout the densification processes. The diffusion of gas at depths near the bottom of the firm is dependent on the extent of alternation of firm microstructural characteristics, which is affected by summer insolation. This link explains the coherent variation observed in the O_2/N_2 ratios in gas trapped in the Vostok [Bender, 2002] and Dome Fuji [Kawamura *et al.*, 2007] ice cores. This link also explains the coherent variation observed in the TAC in Dome Fuji [Kawamura *et al.*, 2004], EPICA Dome C [Raynaud *et al.*, 2007] ice cores. Mechanical persistence of the IHDF determines a depth for the completion of bubble close-off, and consequently determines the duration of the pressure lag between closing/closed bubbles and open channels of pores for a given layer of firm. The pressure lag causes transport of gas molecules until the

pore channels for the vertical diffusion of gas are closed in the IHDF. In this manner, the O_2/N_2 ratio and TAC in deep ice cores form a supporting physical model which can be used to further examine the reliability of the O_2/N_2 ratio and TAC as local insolation proxies used for astronomical dating of deep ice cores [e.g., *Kawamura et al.*, 2007]. The O_2/N_2 -based astronomical time markers have low uncertainty, typically less than 2 ka, as empirically determined by *Kawamura et al.* [2007]. According to the present model, the uncertainty can be diminished if the incidental fluctuation of the O_2/N_2 ratio and TAC values caused by irregularity of the IHDF/ILDF stratification can be removed. This irregularity is introduced by irregularity in surface deposition [*Kameda et al.* 2008]. Either larger samples for each measurement or an increased sampling rate along core depth is required to obtain data that represent larger volume of ice core. It is assumed that there is no time lag requiring correction in the O_2/N_2 -ratio-based age and TAC-based age of the ice core because the properties of the IHDF is imprinted at the surface as an initial effect. The model may need to consider possible additional effects acquired from temperature gradients if vapor transport along the vertical between the neighboring IHDFs and ILDFs significantly modify mechanical properties of the stratified firm and if strength of such modification varies cyclically due to Milankovitch cycle.

We demonstrated that the air enclosure process could be understood only using

high-resolution data at millimeter and centimeter scales. High-resolution data of the distribution of snow/firn types and thickness of layers are needed to better understand how stratigraphy controls air enclosure on the micro-scale. X-ray-absorption microtomography is one important method for the analysis of detailed structure. Also, we demonstrated that measuring dielectric permittivity using an open resonator can also be used to study the structural anisotropy of pores in firn, and is suitable for continuous measurement along firn core samples. The complementary use of both provides a comprehensive understanding of firn structures within polar ice sheets. In addition, we demonstrated that the QMP data measured with the air-sucking method were significantly correlated with data from the other high-resolution measurements. Although we did not employ experimental setup necessary for the real permeability measurement with a typical resolution of ~ 10 cm [e.g., *Albert et al.*, 2000], the QMP data are useful in terms of effective high spatial resolution necessary for the study of the gas transport conditions during bubble close-off.

Future studies are required to better understand and quantitatively model the physical mechanisms outlined in this paper. Particular issues to be addressed include: (i) How does the IHDF evolve in the top few meters of the ice sheet after initial formation? (ii) How do the processes differ at sites with different accumulation environments, i.e.,

spatial variability? The crossover of ρ and the thicknesses of layers constituting the strata are two important keys. (iii) Diffusion of gas molecules within the ice lattice is dependent on temperature [Ikeda-Fukazawa *et al.* (2005)]. How do processes differ at times of different firm temperature? (iv) The densification processes of the ILDF and IHDF should be separately analyzed and formulated in terms of ice bonding of particles, geometrical structure of pores, the COF within firm and possible effects from impurity content. (v) The transport processes, i.e., both permeation and effusion, of air in the ILDF and IHDF and their boundaries should be analyzed and formulated in terms of distribution of pressure within air bubbles, mean distance between closed bubbles and pore channels and temperature in the firm. (vi) X-ray-absorption microtomography may be able to show examples of closing/closed air bubbles, which will help to better understand micro-scale phenomena. (vii) Different measures of summer insolation (for example, peak of summer solstice insolation, integrated insolation over summer or duration of summer) may work differently to the direct insolation effect on the firm metamorphism [e.g., *Huybers and Denton, 2008*]. We need to explore the most effective measures of summer insolation for the surface metamorphism.

Appendix: Crushing events

Destructive deformation associated with vertical crushing events may occasionally occur. Based on unusual $\Delta\varepsilon$ values and the unusually fragmented appearance of the structure in Figure 6(3), the L1-layer in Figure 2(e) at 44.79 m is likely to have undergone such an event. Another sample from 44.75 m depth exhibited similar morphology and interface characteristics. A value of zero for $\Delta\varepsilon$ implies that these layers have lost not only their structural anisotropy but also COF anisotropy. Such conditions can only occur through catastrophic crushing. Crushing may be triggered when the normal stress in z exceeds the fracture stress. V_B are 6.6 and $6.4 \times 10^{-6} \text{ m}^3 \text{ kg}^{-1}$ at 44.75 m and 44.79 m, respectively, and they are much larger than the ordinary values of V_B of $1.3 (2\sigma=1.0) \times 10^{-6} \text{ m}^3 \text{ kg}^{-1}$ at depths shallower than 69.73 m (see section 4.3), implying that the gas-entrapping mechanism for the microbubbles is also extraordinary in these layers.

Over the previous 14 years, members of the ice-coring teams at Dome Fuji have heard low-frequency vibrations originating from deep within the firm, which might be caused by crushing events. The occurrence of such events is infrequent (several occurring throughout the year), and some have lasted for more than 20 seconds. The observers have reported that the sound appeared to spread and propagate over a wide area. *Azuma et al.* [2000] found several unusually isotropic COF layers in the COF data of the Dome Fuji deep core. Such examples are characterized by the median inclination φ approximately

10~20° larger than those of adjacent depths. It is possible that these may have their origin in vertical crushing events.

Notation

TAC Total air content within unit weight of ice at temperature 273.1 K and under pressure at 0.1013 MPa, ml_{STP} kg⁻¹ of ice

ε_v Relative dielectric permittivity along the vertical

ε_h Relative dielectric permittivity along the horizontal

ε Average value of the relative dielectric permittivity over volume ($=|\varepsilon_v/3+2\varepsilon_h/3|$)

assuming that the permittivity is uniaxially anisotropic around the vertical.

$\Delta\varepsilon$ Dielectric anisotropy ($=|\varepsilon_v - \varepsilon_h|$)

QMP Qualitative measure of permeability (also referred to as impermeability [Watanabe *et al.* 1997a] or permeability [Langway *et al.*, 1993]), Torr

z Depth of sample in the ice sheet, m

ρ Bulk density, kg m⁻³

σ_ρ Standard deviation of the bulk density in a sample, kg m⁻³

$[\rho_s]$ Bulk density averaged over a sample, kg m⁻³

$\rho - [\rho_s]$ Bulk density of given depth relative to the averaged value over a sample, kg m⁻³

Δx	Dimension of sample along one horizontal axis, mm
Δy	Dimension of sample along one horizontal axis but orthogonal to Δx , mm
Δz	Dimension of sample along the vertical, mm
l_v	Correlation length along the vertical, mm
l_h	Correlation length along the horizontal, mm
V_B	Volume of isolated air bubbles within unit weight of the firm sample, $\text{m}^3 \text{kg}^{-1}$
R_a	Axial ratio defined as l_v/l_h
V_i/V_p :	Fraction of volume for the isolated air bubbles (V_i) out of volume for the total pore space (V_p) within a sample
z_s	Depth of starting of the normal bubble formation where 5% of V_B is attained with reference to the V_B at z_c , m
z_c	Depth of completion of bubble close-off, m
Δz_c	Variable range for depth of completion of bubble close-off, m
φ	Median inclination, degrees
r	Linear correlation coefficient
α	Significance level ($0 < \alpha < 1$)
Δp	Pressure lag between closed air bubble and channels of open pore
$t(z)$	Age of firm as a function of depth

τ	Duration from the start of bubble close-off in the ILDF until the completion of bubble close-off in the IHDF: $\tau = t(z_c) - t(z_s)$
L	Diffusion length, m
D_n	Diffusion coefficient of molecule of gas n within ice, $\text{m}^2 \text{s}^{-1}$
j_n	Permeation flux of gas n through ice lattice, $\text{mol m}^{-2} \text{s}^{-1}$
X_n	Solubility of gas n in ice lattice, $\text{mol m}_{\text{ice}}^{-3} \text{Pa}^{-1}$
Δp_n	Partial pressure differences of gas n across the ice wall, Pa
x_w	Distance through the ice wall, m
$D_n X_n$	Permeation coefficient, $\text{mol m}_{\text{ice}}^{-1} \text{s}^{-1} \text{Pa}^{-1}$
$\delta(\text{O}_2/\text{N}_2)$	Deviation of O_2/N_2 ratio from present atmosphere, ‰

Acknowledgements

We acknowledge the assistance of S. Takeya of AIST in X-ray absorption microtomography. J.P. Severinghaus and K. Kawamura provided thoughtful comments regarding the manuscript, which improved the manuscript considerably. K. Fujita and T. Shiraiwa allowed S.F. to access unpublished field data of snow properties at Dome Fuji for this study. A. Miyamoto, T. Kameda and Y. Iizuka assisted S.F. in the interpretation of

previous data and provided valuable comments. S. Surdyk assisted us in the computation of volumes for isolated air bubbles from the data of the X-ray absorption microtomography. Thanks are extended to J. Kipfthuhl and J. Freitag for discussions with S.F. under the Japan (JSPS) – Germany (DFG) Research Cooperative Program. This research was supported by a Grant-in-Aid for Creative Scientific Research (No. 14GS0202) from the Japanese Ministry of Education, Culture, Sports, Science and Technology.

References

- EPICA community members (2004), Eight glacial cycles from an Antarctic ice core, *Nature*, 429(6992), 623-628, doi: 10.1038/nature02599.
- Albert, M. R., E. F. Shultz and F. E. Perron (2000), Snow and firn permeability at Siple Dome, Antarctica, *Ann. Glaciol.*, 31, 353-356.
- Alley, R. B. (1987a), Texture of polar firn for remote sensing, *Ann. Glaciol.*, 9, 1-4.
- Alley, R. B. (1987b), Firn densification by grain-boundary sliding: a first model, *J. Phys. (Paris)*, 48(colloq. C1), 249-254. (Supplement au 243).
- Alley, R. B. (1988), Concerning the deposition and diagenesis of strata in polar firn, *J. Glaciol.*, 34(118), 283-290.
- Alley, R. B., E. S. Saltzman, K. M. Cuffey and J. J. Fitzpatrick (1990), Summertime formation of depth hoar in central Greenland, *Geophys. Res. Lett.*, 17(12), 2393-2396.
- Anderson, D. L., and C. S. Benson (1963), The densification and diagenesis of snow, in *Ice and Snow*, edited by W. D. Kingery, pp. 391-411, M.I.T. Press, Cambridge, Massachusetts.
- Arnaud, L., V. Lipenkov, J.-M. Barnola, M. Gay and P. Duval (1998), Modelling of the densification of polar firn: characterization of the snow-firn transition, *Ann. Glaciol.*, 26, 39-44.

Azuma, N., and A. Higashi (1985), Formation processes of ice fabric pattern in ice sheets,

Ann. Glaciol., 6, 130-134.

Azuma, N. (1994), A flow law for anisotropic ice and its application to ice sheets, *Earth*

Planet. Sci. Lett., 128, 601-614.

Azuma, N. (1995), A flow law for anisotropic polycrystalline ice under uniaxial

compressive deformation, *Cold Reg. Sci. Technol.*, 23, 137-147.

Azuma, N., T. Kameda, Y. Nakayama, Y. Tanaka, H. Yoshimi, T. Furukawa and Y. Ageta

(1997), Glaciological data collected by the 36th Japanese Antarctic Research

Expedition during 1995-1996, *JARE Data Reports (National Institute of Polar*

Research, Tokyo), 223 (*GLACIOLOGY* 26), 83.

Azuma, N., Y. Wang, Y. Yoshida, H. Narita, T. Hondoh, H. Shoji and O. Watanabe (2000),

Crystallographic analysis of the Dome Fuji ice core, in *Physics of Ice Core Records*,

edited by T. Hondoh, pp. 45-61, Hokkaido University Press, Sapporo.

Battle, M., M. Bender, T. Sowers, P. P. Tans, J. H. Butler, J. W. Elkins, J. T. Ellis, T.

Conway, N. Zhang, P. Lang and A. D. Clarke (1996), Atmospheric gas concentrations

over the past century measured in air from firn at the South Pole, *Nature*, 383(6597),

231-235.

Bender, M. L., M. Bender, T. Sowers, P. P. Tans, J. H. Butler, J. W. Elkins, J. T. Ellis, T.

- Conway, N. Zhang, P. Lang and A. D. Clarke (1994), Changes in the O₂/N₂ ratio of the atmosphere during recent decades reflected in the composition of air in the firm at Vostok Station, Antarctica, *Geophys. Res. Lett.*, *21*(3), 189-192.
- Bender, M. L., T. Sowers and V. Lipenkov (1995), On the concentration of O₂, N₂, and air in trapped gases from ice cores, *J. Geophys. Res.*, *100*(D9), 18,651-18,660.
- Bender, M. L. (2002), Orbital tuning chronology for the Vostok climate record supported by trapped gas composition, *Earth Planet. Sci. Lett.*, *204*(1-2), 274-289.
- Colbeck, S. C. (1989), Snow-crystal growth with varying surface temperatures and radiation penetration, *J. Glaciol.*, *35*, 23-29.
- Courville, Z. R., M. R. Albert, M. A. Fahnestock, L. M. Cathles IV, and C. A. Shuman (2007), Impacts of an accumulation hiatus on the physical properties of firm at a low-accumulation polar site, *J. Geophys. Res.*, *112*, F02030, doi:10.1029/2005JF000429
- Dang, H., C. Genthon and E. Martin (1997), Numerical modeling of snow cover over polar ice sheets, *Ann. Glaciol.*, *25*, 170-176.
- Endo, Y., and K. Fujiwara (1973), *Characteristics of the Snow Cover in East Antarctica Along the Route of the JARE South Pole Traverse and Factors Controlling such Characteristics*, 38 pp., Polar Research Center, National Science Museum, Tokyo.

- Freitag, J., F. Wilhelms and S. Kipfstuhl (2004), Microstructure-dependent densification of polar firn derived from X-ray microtomography, *J. Glaciol.*, 50(169), 243-250.
- Fujita, S., H. Enomoto, T. Kameda, H. Motoyama and S. Sugiyama (2008), Changes of surface snow density in a summer in the Antarctic Dome Fuji region, paper presented at SCAR/IASC IPY Open Science Conference, St. Petersburg, Russia, 8-11 July, Abstract Volume, 273-274.
- Gerland, S., H. Oerter, J. Kipfstuhl, F. Wilhelms, H. Miller and W. D. Miners (1999), Density log of a 181 m long ice core from Berkner Island, Antarctica, *Ann. Glaciol.*, 29, 215-219.
- Gow, A. J., and R. O. Ramseier (1963), Age hardening of snow at the South Pole, *J. Glaciol.*, 4(35), 521-536.
- Gow, A. J. (1975), Time-temperature dependence of sintering in perennial isothermal snowpacks, *IAHS*, 114, 25-41.
- Goujon, C., J.-M. Barnola, and C. Ritz (2003), Modeling the densification of polar firn including heat diffusion: Application to close-off characteristics and gas isotopic fractionation for Antarctica and Greenland sites, *J. Geophys. Res.*, 108 (D24), 4792, doi:10.1029/2002JD003319.
- Hondoh, T., H. Narita, A. Hori, M. Fujii, H. Shoji, T. Kameda, S. Mae, S. Fujita, T. Ikeda,

- H. Fukazawa, T. Fukumura, N. Azuma, Y. Wong, K. Kunio, O. Watanabe and H. Motoyama (1999), Basic analyses of Dome Fuji deep ice core, part 2: physical properties, *Polar Meteorol. Glaciol.*, *13*, 90-98.
- Hondoh, T. (2000), *Physics of Ice Core Records*, 459 pp., Hokkaido University Press, Sapporo.
- Hori, A., K. Tayuki, H. Narita, T. Hondoh, S. Fujita, T. Kameda, H. Shoji, N. Azuma, K. Kamiyama, Y. Fujii, H. Motoyama and O. Watanabe (1999), A detailed density profile of the Dome Fuji (Antarctica) shallow ice core by X-ray transmission method, *Ann. Glaciol.*, *29*, 211-214.
- Huber, C., U. Beyerle, M. Leuenberger, J. Schwander, R. Kipfer, R. Spahni, J. P. Severinghaus and K. Weiler (2006), Evidence for molecular size dependent gas fractionation in firn air derived from noble gases, oxygen, and nitrogen measurements, *Earth Planet. Sci. Lett.*, *243*, 61-73, doi:10.1016/j.epsl.2005.12.036.
- Hutterli, M.A., J. Freitag, S. Kipfstuhl, M. Schneebeli, and R. Röthlisberger (2008), Orbital tuning of ice core age scales: Improvements with a physically based model, *Geophysical Research Abstracts*, *EGU General Assembly 2008*, *10*, EGU2008-A-04142.
- Huybers, P., and G. Denton (2008), Antarctic temperature at orbital timescales controlled

- by local summer duration, *Nature Geoscience*, 1 (11), 787-792, doi: 10.1038/ngeo311.
- Iizuka, Y., Y. Fujii, N. Hirasawa, T. Suzuki, H. Motoyama, T. Furukawa, and T. Hondoh (2004), SO₄²⁻ minimum in summer snow layer at Dome Fuji, Antarctica, and the probable mechanism, *J. Geophys. Res.*, 109 (D04307), doi:10.1029/2003JD004138.
- Iizuka, Y., T. Hondoh, and Y. Fujii (2006), Na₂SO₄ and MgSO₄ salts during the Holocene period derived by high-resolution depth analysis of a Dome Fuji ice core *J. Glaciol.*, 52 (176), 58-64.
- Ikeda-Fukazawa, T., T. Hondoh, T. Fukumura, H. Fukazawa and S. Mae (2001), Variation in N₂/O₂ ratio of occluded air in Dome Fuji Antarctic ice, *J. Geophys. Res.*, 106(D6), 17,799-17,810.
- Ikeda-Fukazawa, T., K. Kawamura and T. Hondoh (2004), Mechanism of molecular diffusion in ice crystals, *Mol. Simulat.*, 30(13-15), 973-979, doi: 10.1080/08927020410001709307.
- Ikeda-Fukazawa, T., K. Fukumizu, K. Kawamura, S. Aoki, T. Nakazawa and T. Hondoh (2005), Effects of molecular diffusion on trapped gas composition in polar ice cores, *Earth Planet. Sci. Lett.*, 229, 183-192, doi:10.1016/j.epsl.2004.11.011.
- Ikeda, T., H. Fukazawa, S. Mae, L. Pepin, P. Duval, B. Champagnon, V. Y. Lipenkov and T. Hondoh (1999), Extreme fractionation of gases caused by formation of clathrate

- hydrates in Vostok Antarctic ice, *Geophys. Res. Lett.*, 26(1), 91-94.
- Ishijima, K., S. Sugawara, K. Kawamura, G. Hashida, S. Morimoto, S. Murayama, S. Aoki and T. Nakazawa (2007), Temporal variations of the atmospheric nitrous oxide concentration and its $\delta^{15}\text{N}$ and $\delta^{18}\text{O}$ for the latter half of the 20th century reconstructed from firn air analyses, *J. Geophys. Res.*, 112, D03305, doi:10.1029/2006JD007208.
- Jones, R. G. (1976), The measurement of dielectric anisotropy using a microwave open resonator, *J. Phys. D: Appl. Phys.*, 9, 819-827.
- Kameda, T., N. Azuma, T. Furukawa, Y. Ageta and S. Takahashi (1997), Surface mass balance, sublimation and snow temperatures at Dome Fuji Station, Antarctica in 1995, *Proc. NIPR Symp. Polar Meteorol. Glaciol.*, 11, 35-50.
- Kameda, T., H. Motoyama, S. Fujita and S. Takahashi (2008), Temporal and spatial variability of surface mass balance at Dome Fuji, East Antarctica, by the stake method from 1995 to 2006, *J. Glaciol.*, 54(184), 107-116.
- Kawamura, K., T. Nakazawa, S. Aoki, Y. Fujii, O. Watanabe and J. Severinghaus (2004), Close resemblance between local summer insolation, O_2/N_2 and total air content from the Dome Fuji ice core, Antarctica, paper presented at Eos Trans. AGU, 85(47), Fall Meet. Suppl., Abstract C33C-0356.

- Kawamura, K., J. P. Severinghaus, S. Ishido, S. Sugawara, G. Hashida, H. Motoyama, Y. Fujii, S. Aoki and T. Nakazawa (2006), Convective mixing of air in firn at four polar sites, *Earth Planet. Sci. Lett.*, 244(34), 672-682, doi:10.1016/j.epsl.2006.02.017.
- Kawamura, K., F. Parrenin, L. Lisiecki, R. Uemura, F. Vimeux, J. P. Severinghaus, M. A. Hutterli, T. Nakazawa, S. Aoki, J. Jouzel, M. E. Raymo, K. Matsumoto, H. Nakata, H. Motoyama, S. Fujita, K. Azuma, Y. Fujii and O. Watanabe (2007), Northern Hemisphere forcing of climatic cycles over the past 360,000 years implied by accurately dated Antarctic ice cores, *Nature*, 448(7156), 912-916, doi:10.1038/nature06015.
- Koerner, R. M. (1971), A stratigraphic method of determining the snow accumulation rate at Plateau Station, Antarctica, and application to South Pole-Queen Maud Land Traverse 2, 1965-1966, in *Antarctic Ice Studies II*, edited by A. P. Crary, pp. 225-238, American Geophysical Union, Washington D.C.
- Kojima, K. (1967), Densification of seasonal snow cover, in *Physics of Snow and Ice*, edited by H. Oura, pp. 929-952, Inst. Low Temp. Sci., Hokkaido Univ., Sapporo.
- Komiyama, B., M. Kiyokawa and T. Matsui (1991), Open resonator for precision dielectric measurements in the 100 GHz band, *IEEE Trans. Microwave Theory Tech.*, 39, 1792-1796.

- Kovacs, A., A. J. Gow and R. M. Morey (1995), The in-situ dielectric constant of polar firn revisited, *Cold Reg. Sci. Technol.*, 23(3), 245-256.
- Landais, A., J. M. Barnola, K. Kawamura, N. Caillon, M. Delmotte, T. Van Ommen, G. Dreyfus, J. Jouzel, V. Masson-Delmotte, B. Minster, J. Freitag, M. Leuenberger, J. Schwander, C. Huber, D. Etheridge and V. Morgan (2006), Firn air $\delta^{15}\text{N}$ in model polar sites and glacial-interglacial ice: a model-data mismatch during glacial periods in Antarctica?, *Quat. Sci. Rev.*, 25, 49-62, doi:10.1016/j.quascirev.2005.06.007.
- Langway, C. C. Jr., H. Shoji, A. Mitani and H. B. Clausen (1993), Transformation process observations of polar firn to ice, *Ann. Glaciol.*, 18, 199-202.
- Li, J., and H. J. Zwally (2004), Modeling the density variation in the shallow firn layer, *Ann. Glaciol.*, 38(309-313).
- Lipenkov, V. Y., Air bubbles and air-hydrate crystals in the Vostok ice core, in *Physics of Ice Cores Records*, edited by T. Hondoh, pp. 327–358, Hokkaido Univ. Press, Sapporo, Japan, 2000.
- Lytle, V. I., and K. C. Jezek (1994), Dielectric permittivity and scattering measurements of Greenland firn at 26.5-40 GHz, *IEEE Trans. Geosci. Remote Sensing*, 32(2), 290-295.
- Maeno, N., and T. Ebinuma (1983), Pressure sintering of ice and its implications to the

- densification of snow at polar glaciers and ice sheets, *J. Phys. Chem.*, *87*, 4103-4110.
- Martinerie, P., D. Raynaud, D. M. Etheridge, J.-M. Barnola and D. Mazaudier (1992), Physical and climatic parameters which influence the air content in polar ice, *Earth Planet. Sci. Lett.*, *112*(1-4), 1-13.
- Matsuoka, T., S. Fujita, S. Morishima and S. Mae (1997), Precise measurement of dielectric anisotropy in ice Ih at 39 GHz., *J. Appl. Phys.*, *81*(5), 2344-2348.
- Matsuoka, T., S. Mae, H. Fukazawa, S. Fujita and O. Watanabe (1998), Microwave dielectric properties of the ice core from Dome Fuji, Antarctica, *Geophys. Res. Lett.*, *25*(10), 1573-1576.
- Motoyama, H., H. Enomoto, M. Miyahara and O. Watanabe (1995), Shallow ice coring and borehole casing at Dome Fuji Station, East Antarctica., *Nankyoku Shiryo (Antarctic Record)*, *39*, 189-197.
- Paterson, W.S.B. (1991), Why ice-age ice is sometimes "soft", *Cold Reg. Sci. Technol.*, *20*, 75-98
- Paterson, W. S. B. (1994), *The Physics of Glaciers*, Third ed., 480 pp., Pergamon.
- Petit, J. R., J. Jouzel, D. Raynaud, N. I. Barkov, J.-M. Barnola, I. Basile, M. Bender, J. Chappellaz, M. Davis, G. Delaygue, M. Delmotte, V. M. Kotlyakov, M. Legrand, V. Y. Lipenkov, C. Lorius, L. Pepin, C. Ritz, E. Saltzman and M. Stievenard (1999),

- Climate and atmospheric history of the past 420,000 years from the Vostok ice core, Antarctica, *Nature*, 399, 429-436.
- Pfeffer, W. T., and R. Mrugala (2002), Temperature gradient and initial snow density as controlling factors in the formation and structure of hard depth hoar, *J. Glaciol.*, 48(163), 485-494.
- Polder, D., and J. H. V. Santen (1946), The effective permeability of mixtures of solids, *Physica XII*, 5, 257-271.
- Ramseier, R. O., and G. W. Sander (1966), Temperature dependence and mechanics of sintering, *U.S. Cold Regions Res. Eng. Lab., Res. Rep.*, 189, 15 pp.
- Ramseier, R. O., and C. Keeler (1967), The sintering process in snow, *J. Glaciol.*, 6(45), 421-424.
- Raynaud, D., V. Lipenkov, B. Lemieux-Dudon, P. Duval, M.-F. Loutre and N. Lhomme (2007), The local insolation signature of air content in Antarctic ice. A new step toward an absolute dating of ice records, *Earth Planet. Sci. Lett.*, 261(3-4), 337-349, doi:10.1016/j.epsl.2007.06.025.
- Rick, U., and M.R. Albert (2004), Microstructure and permeability in the near-surface firn near a potential US deep-drilling site in West Antarctica, *Ann. Glaciol.*, 39, 62-66, doi: 10.3189/172756404781814320.

- Schwander, J., and B. Stauffer (1984), Age difference between polar ice and the air trapped in its bubbles, *Nature*, *311*, 45-47.
- Schwander, J., J.-M. Barnola, C. Andrie, M. Leuenberger, A. Ludin, D. Raynaud and B. Stauffer (1993), The age of the air in the firn and the ice at Summit, Greenland, *J. Geophys. Res.*, *98*(D2), 2831-2838.
- Schwander, J., T. Sowers, J.-M. Barnola, T. Blunier, A. Fuchs and B. Malaize (1997), Age scale of the air in the summit ice: Implication for glacial-interglacial temperature change, *J. Geophys. Res.*, *102*(D16), 19483-19493.
- Severinghaus, J. P., and M. O. Battle (2006), Fractionation of gases in polar ice during bubble close-off: New constraints from firn air Ne, Kr and Xe observations, *Earth Planet. Sci. Lett.*, *244*(1-2), 474-500, doi:10.1016/j.epsl.2006.01.032.
- Shiraiwa, T., H. Shoji, T. Saito, K. Yokoyama and O. Watanabe (1996), Structure and dielectric properties of surface snow along the traverse route from coast to Dome Fuji Station, Queen Maud Land, Antarctica., *Proc. NIPR Symp. Polar Meteorol. Glaciol.*, *10*, 1-12.
- Sihvola, A. H., and J. A. Kong (1988), Effective permittivity of dielectric mixtures, *IEEE Trans. Geosci. Remote Sensing*, *26*(4), 420-429.
- Steffensen, P. J. (1966), Some considerations of snow metamorphism in the Antarctic ice

- sheet in the light of crystal studies, in *Physics of Snow and Ice*, edited by H. Oura, pp. 725-740, Inst. Low Temp. Sci., Hokkaido Univ., Sapporo.
- Sugawara, S., K. Kawamura, S. Aoki, T. Nakazawa and G. Hashida (2003), Reconstruction of past variations of $\delta^{13}\text{C}$ in atmospheric CO_2 from its vertical distribution observed in the firn at Dome Fuji, Antarctica, *Tellus*, 55(B), 159-169.
- Suwa, M., and M. Bender (2008), O_2/N_2 ratios of occluded air in the GISP2 ice core, *J. Geophys. Res.*, 113 (D11119), doi:10.1029/2007JD009589.
- Vallese, F., and J. A. Kong (1981), Correlation function studies for snow and ice, *J. Appl. Phys.*, 52(8), 4921-4925.
- Watanabe, O., W. Shimada, H. Narita, A. Miyamoto, K. Tayuki, T. Hondoh, T. Kawamura, S. Fujita, H. Shoji, H. Enomoto, T. Kameda, K. Kawada and K. Yokoyama (1997a), Preliminary discussion of physical properties of the Dome Fuji shallow ice core in 1993, Antarctica, *Proc. NIPR Symp. Polar Meteorol. Glaciol.*, 11, 1-8.
- Watanabe, O., Y. Fujii, H. Motoyama, T. Furukawa, H. Shoji, H. Enomoto, T. Kameda, H. Narita, R. Naruse, T. Hondoh, S. Fujita, S. Mae, N. Azuma, S. Kobayashi, M. Nakawo, Y. Ageta (1997b), Preliminary study of ice core chronology at Dome Fuji Station, Antarctica, *Proc. NIPR Symp. Polar Meteorol. Glaciol.*, 11, 9-13.
- Watanabe, O., K. Kamiyama, H. Motoyama, Y. Fujii, H. Shoji and K. Satow (1999), The

paleoclimate record in the ice core at Dome Fuji Station, East Antarctica, *Ann. Glaciol.*, 29, 176-178.

Watanabe, O., J. Jouzel, S. Johnsen, F. Parrenin, H. Shoji and N. Yoshida (2003), Homogeneous climate variability across East Antarctica over the past three glacial cycles, *Nature*, 422, 509-512.

Wenk, H.-R. (1985), *Preferred Orientation in Deformed Metals and Rocks: An Introduction to Modern Texture Analysis*, 610 pp., Academic Press, Inc.

Zhou, Y., N. Azuma and T. Kameda (2002), A stratification model of surface snow at Dome Fuji Station, Antarctica, *Polar Meteorol. Glaciol.*, 16, 61-73.

Figures

Figure 1: Topographic map of Antarctica. Surface elevation data are from ERS-1 radar altimetry. Stars indicate locations of sites mentioned in the text.

Figure 2: Dielectric permittivity and density for the ten samples (a) to (j) given in Table 2.

Open circles and solid circles indicate ϵ_v and ϵ_h , respectively, using the upper left axis.

Solid triangles indicate $\Delta\epsilon$ ($=|\epsilon_v - \epsilon_h|$) using the right axis. Density ρ (kg m^{-3}) is shown

using the lower left axis. The gray dotted line is the 1-mm resolution density. Open

squares show Gaussian-weighted average density with a half-power width of ~ 22 mm to

give the same resolution as the dielectric measurements. For three samples (g)-(i), the

qualitative measure of permeability, QMP (Torr), (see sections 2.5, 3.5 and 4.3), of the

core measured previously are given [Watanabe *et al.*, 1997a], using the middle left axis.

The impermeable and free levels are 0 and 760 Torr, respectively. Data on a different

scale are shown in Figures 3(iii) and 9(i). Vertical dotted lines indicate depths where pairs

of $\Delta\epsilon$ dips and ρ bumps occur. “L1” in (e) indicates an unusual layer where it is proposed

that $\Delta\epsilon$ is zero. We discuss plausible causes of zero $\Delta\epsilon$ in the text (see Appendix). Arrows

with letters “C” indicate depths at which COF measurements were performed by the

X-ray diffraction method. Arrows with letters “T” and numbers indicate depths where

X-ray absorption tomography was undertaken. These results are presented in Figure 6.

Figure 3: General trends in the physical properties over the entire depth range of the ice core. (i) Dots show ρ (left axis) for the ten samples (a)-(j) labeled in Table 2 and Figure 2.

The solid line represents bulk density measurements [*Watanabe et al.*, 1997a]. Solid circles and open circles show the standard deviation, σ_ρ , of density for every 1.0 m or less, with the right axis showing the magnitude of variation within each sample. Solid circles

show data from the present study and an earlier study [*Hori et al.*, 1999]. Open circles show data from an ice core drilled at Dome Fuji in 1999 (A. Hori, unpublished data).

Solid triangles are from a 3-m-deep pit in 2004 (K. Fujita, unpublished data). Open triangles are from a 4-m-deep pit in 2007 (unpublished data). Dotted line represents

suggested mean tendency of σ_ρ . σ_ρ has a local minimum at a depth and density of

($z_1 \sim 40-50$ m; $\rho_1 = 630$ kg m⁻³) and a local maximum at ($z_2 \sim 60-70$; $\rho_2 = 720$). The bubble

close-off depth/density is ($z_3 = 104$; $\rho_3 = 830$) ([*Watanabe et al.*, 1997a] and Figure 9(ii)).

Dashed lines are shown to emphasize the coordinates of the points (z_i and ρ_i , $i=1\sim 3$) in the

graph. (ii) Open circles and solid circles show ε_v and ε_h , respectively, on the left axis.

Crosses show $\Delta\varepsilon$ on the right axis. (iii) Left axis shows mean tendency of grain diameter

measured by *Watanabe et al.* [1997a]. A minimum is found at ~ 65 m. Right axis shows

the QMP (Torr) (see section 4.3). The depths of samples (g), (h) and (i) in Table 2 and Figure 2 are indicated with arrows. (iv) The geometric structure of the firn was analyzed using X-ray absorption tomography in Figure 6. The ordinate is the “mean free path” (mm) which is the mean continuous length in ice or pore space without obstruction, calculated using the 3-D volume data. Note that data in layer L1 in Figure 2(e) were excluded because an anomaly, presumably formed by a crushing event (see Appendix), which interrupts the continuous tendency of the physical properties within the firn.

Figure 4: Distribution of $\Delta\varepsilon$ versus ρ for the ten samples labeled in Table 2 and Figure 2. ρ is averaged from the 1-mm resolution data so that it has the same resolution as $\Delta\varepsilon$ (see Figure 2). Open circles and open triangles are used to discriminate between neighboring samples. The dotted line is the fitted curve to a quadratic function for the entire data and each solid line is the linear fit for each sample each sample. The dashed curve and the shaded area at the bottom indicate values of $\Delta\varepsilon$ for ice with the perfectly vertical c-axis and the variable range of $\Delta\varepsilon$ caused by the crystal orientation fabrics, respectively. In the shallow range, we observe a positive correlation between $\Delta\varepsilon$ and ρ , while a negative correlation was dominant at a deeper range (see Figure 5). This finding suggests that firn with smaller $\Delta\varepsilon$ deforms more readily.

Figure 5: Correlations (r) between ρ and $\Delta\varepsilon$ (solid squares) and between ε and $\Delta\varepsilon$ (open circles) for the 10 samples at variable depth z (m) given in Table 2 and Figure 2. The correlation between ρ and $\Delta\varepsilon$ decreased from ~ 0.9 to ~ -0.4 from a depth of ~ 10 m to over 100 m, and the correlation between ε and $\Delta\varepsilon$ also decreased from ~ 0.7 to ~ -0.4 from a depth of ~ 10 m to over 100 m. Exponential fit was used to express suggested tendencies.

Figure 6: Results of the X-ray absorption microtomography. Five examples were selected from 23 measurements. For each sample, one vertical-section image and one horizontal-section image is shown, with each panel showing an area of 10 mm x 10 mm. White and black areas represent ice and pore spaces, respectively. For each sample, depth z , density ρ , dielectric anisotropy $\Delta\varepsilon$, and correlation length [Vallese and Kong, 1981] of pore space along the vertical and along the horizontal (l_v and l_h , respectively) were found.

Figure 7: Relationship between axial ratio, R_a , of the pore space geometry and $\Delta\varepsilon$. R_a is defined as l_v/l_h and was calculated for the 23 X-ray absorption microtomography measurements. The numbers near marker symbols are depths (m) of the samples. Results from two samples at 44.75-m and 44.79-m depth (see Appendix) are shown as solid

circles. R_a and $\Delta\varepsilon$ are positively correlated except at these two points. A linear regression line is given as a dotted line. When R_a is 1, $\Delta\varepsilon$ is ~ 0.01 . We suggest that this residual $\Delta\varepsilon$ is an average COF component of $\Delta\varepsilon$.

Figure 8: Results of crystal orientation fabric measurement using the X-ray diffraction method. The volume-weighted distribution of the c-axes was expressed by the median inclination angle φ , which shows the median alignment value of the c-axes. The abscissa is density relative to the mean value within each sample, $\rho-[\rho_s]$. The numbers near marker symbols indicate the depths (m) of samples. Different marker symbols show results from three different depth ranges. Pairs of neighboring depths where density is different are joined by lines to highlight the contrasting values of φ , dependent on the sign of $\rho-[\rho_s]$.

Figure 9: (i) The qualitative measure of permeability, QMP, in the firn core at depths (m) in the bubble formation zone in the firn core. The QMP was measured by *Watanabe et al.* [1997a] using an air-vacuum system. The diameter of the air-intake is 12 mm. The impermeable and free levels are 0 and 760 Torr, respectively. Near the bubble close-off depth, the upper and the lower limits of the QMP are delineated using dashed lines. The

shallowest impermeable sample portion appears at 100.3 m but sequences of many impermeable sample portions only appear below ~ 104 m. Down to 104 m, the core is still permeable. Three depths, FA1-3, show where the firn-air sampling was conducted in the borehole at Dome Fuji in 1999 [Ishijima *et al.*, 2007; Kawamura *et al.*, 2006; Sugawara *et al.*, 2003]. Firn-air could be sampled down to FA2, but not at FA3. At Dome Fuji, the bubble close-off is complete at the depth where the upper limit of the QMP fluctuations reach zero. The depths of the samples (h) and (i) in Table 2 and Figure 2 are shaded. (ii) Bubble volume in the firn ice [Hondoh *et al.*, 1999], found using a method similar to that developed by Schwander and Stauffer [1984] based on the ideal gas law. Air bubbles isolated from air channels are formed mostly in the depth range to ~ 104 m. Error bars represent σ of values based on repetitive measurements for each sample.

Figure 10: QMP of the core sample (h) versus $\Delta\varepsilon$, ρ and ε . “ r ” in each panel gives the linear correlation coefficient. The QMP has a better correlation with $\Delta\varepsilon$ than that with ρ .

Figure 11: Schematic diagram of the proposed mechanism for the modulation of conditions for gas diffusion near the bottom of firn in the ice sheet as a result of variations in local insolation. The common abscissa for the three graphs is z , where z_s and z_c are the

starting and completion depths of bubble formation and bubble close-off, respectively. In the present ice sheet at Dome Fuji, z_s is ~ 78 m, defined as a depth where 5% of V_B is attained with reference to the V_B at z_c . z_c is ~ 104 m. (i) Schematic graph of the depth-permeability relationship such as Figure 9(i), which shows how changes in the upper limit of the permeability peaks translate into changes in the depth of completion of bubble close-off. (ii) Schematic graph for depth- V_B relationship such as Figure 9(ii). Bubble formation in the IHDF tends to be retarded in ages of intense insolation. It affects the duration available for gas transportation from closed/closing air bubbles to channels of open pores. (iii) Schematic graph for depth- $\partial V_B/\partial z$ relationship, which shows increasing rate of volume of isolated air bubbles with depth. The depth- $\partial V_B/\partial z$ relationship constitutes a peak, which broadens when retardation of bubble formation in the IHDF occurs. At depths between z_s and z_c and during a period between $t(z_s)$ and $t(z_c)$, there are pressure lags Δp , between closing/closed bubbles and channels of open pores.

Tables

Table 1: Characteristics of the measurement methodology used to examine the Dome Fuji ice core in the present study

Method	Text Section and references	Target physical properties	Continuous/spot? Resolution in depth	Shape and size of the sample ^a
Density measurement using the X-ray transmission method	2.1., [Hori <i>et al.</i> , 1999]	Bulk density, ρ	Continuous ~1 mm	Slab $\Delta x=25$ mm, $\Delta y=60$ mm, $\Delta z= \sim 500$ mm
Dielectric permittivity tensor measurement using an open resonator method	2.2., [Jones, 1976; Matsuoka <i>et al.</i> , 1997; Matsuoka <i>et al.</i> , 1998]	Dielectric permittivity along the vertical and horizontal, ϵ_v and ϵ_h ; Dielectric anisotropy, $\Delta\epsilon = \epsilon_v - \epsilon_h $	Continuous ~22 mm (see text)	Slab $\Delta x= 5$ mm, $\Delta y=60$ mm, $\Delta z= \sim 500$ mm
Geometrical structure using X-ray absorption microtomography method	2.3., [Freitag <i>et al.</i> , 2004]	3-D firm structure (e.g., axial ratio, R_a , mean free path, volume of isolated bubbles and open pores etc.)	Spot 13.5 mm ^b	Core cylinder, 15 mm diameter in the horizontal, $\Delta z= 15$ mm
Pole figure measurements using X-ray diffraction method	2.4., [Wenk, 1985]	Crystal orientation fabrics as volume weighted quantity (e.g., Median inclination, φ , etc.)	Spot 1 mm ^c	Slab $\Delta x=30$ mm, $\Delta y=60$ mm, $\Delta z= 7$ mm
Qualitative measure of permeability using an air-vacuum system	2.5., [Langway <i>et al.</i> , 1993; Watanabe <i>et al.</i> , 1997]	Qualitative measure of permeability (QMP) ^d	Continuous >12 mm ^e	Bulk core with a flat surface, $\Delta x=35$ mm, $\Delta y=70$ mm, $\Delta z=500$ mm

^a Δx , Δy and Δz are sample dimensions along the horizontal axis, orthogonal axis in the horizontal, and the vertical, respectively.

^b 13.5 mm is the size of the 3-D image in which pixels have a resolution of 0.025 mm.

^c The incident depth of X-rays into the 7-mm-thick specimens.

^d See text section 4.3.

^e 12 mm is diameter of the top of the air-intake for the vacuum pump. Effective resolution of the QMP resolution is slightly larger than that. However, the values reflect firm property mostly in the very vicinity of the air-intake.

Table 2: Sample depth and statistics for density, ε and $\Delta\varepsilon$, for the Dome Fuji ice core

Sample ID	Depth (m)		Density (kg m ⁻³)		ε ^a		$\Delta\varepsilon$		Max.	Min.
	Top	Bottom	Mean	SD ^b	Mean	SD.	Mean	SD		
a	9.59	9.83	418	12	1.88	0.02	0.054	0.009	0.068	0.034
b	12.32	12.73	469	12	1.93	0.02	0.045	0.012	0.069	0.022
c	24.53	24.89	573	6	2.11	0.02	0.026	0.007	0.043	0.011
d	28.81	29.22	590	8	2.19	0.01	0.030	0.017	0.045	0.020
e	44.40	44.83	625	7	2.32	0.02	0.015	0.013	0.037	0 ^c
f	54.08	54.40	687	9	2.46	0.02	0.021	0.004	0.029	0.008
g	69.40	69.78	746	7	2.62	0.03	0.020	0.008	0.040	0.010
h	87.57	88.02	787	7	2.76	0.04	0.014	0.003	0.018	0.005
i	103.59	103.92	837	4	2.91	0.01	0.008	0.004	0.013	0.006
j	112.13	112.57	869	7	2.96	0.02	0.009	0.003	0.014	0 ^c

^a ε is an average value over volume ($=|\varepsilon_v/3+2\varepsilon_h/3|$), assuming that the dielectric permittivity has uniaxial anisotropy.

^b SD: Standard deviation

^c The value is less than 0.003.

Table 3: Physical features and 3-D firm structure of the five samples in Figure 6, extracted from X-ray absorption microtomography data

Sample ID	z (m)	ρ (kg m ⁻³)	$\Delta\epsilon$	l_v ^a (mm)	l_h ^a (mm)	R_a ^b	V_i/V_p ^c (%)	V_B ^d (x 10 ⁻⁶ m ³ kg ⁻¹)
T1	12.44	481	0.057	0.33	0.28	1.18	0.1	0.9
T2	29.12	588	0.025	0.32	0.30	1.07	0.3	1.9
T3	44.79	628	0 ^e	0.26	0.18	1.44	1.0 ^f	6.4 ^f
T4	69.73	757	0.012	0.29	0.28	1.04	0.5	1.4
T5	103.84	844	0.007	0.25	0.25	1.00	44.8 ^g	55.5 ^e

^a l_v and l_h are correlation-lengths of pore space [e.g., *Vallese and Kong*, 1981] both in the vertical direction and in the horizontal direction.

^b R_a the axial ratio (R_a), defined as l_v/l_h .

^c V_i/V_p is fraction of volume for the isolated air bubbles (V_i) out of volume for the total pore space (V_p) within a sample. Isolation here means only from the air outside of the cylindrical sample used for the measurement.

^d V_B is volume of isolated air bubbles within a unit weight of the firm sample.

^e The value is less than 0.003.

^f This sample may be affected by crushing events, see Appendix.

^g In the real firm of the ice sheet, V_i/V_p for the sample T5 should be much larger because here many bubbles at the surface of the cylindrical sample are counted as open pores. This effect may also weakly occur in the other samples.

Table 4: Variable range of values related to the local insolation modulation of gas transport conditions at Dome Fuji for a period from 350 ka BP to present.

Parameters	Unit	Max.	Min.	Variable range	
					%
Local insolation at 77 °S on Dec. 11 ^a	W m ⁻²	~610	~470	~140	~30 ^b
$\delta(\text{O}_2/\text{N}_2)$ ^{a, c}	‰	~ -13 ^d	~ -25 ^d	~12	-
TAC ^a	ml _{STP} kg ⁻¹ of ice ^e	~91 ^d	~85 ^d	~6	~7
Variable range of depth for bubble formation	m	-	-	~2 ^f	~8 ^g

^a Data are from *Kawamura et al.* [2007] and *Kawamura et al.* [2004]

^b Relative to the minimum value of the local insolation

^c Deviation of O₂/N₂ ratio from present atmosphere

^d The maximum and the minimum correspond to the minimum and the maximum of the local insolation.

^e STP means temperature at 273.1 K and pressure at 0.1013 MPa.

^f Δz_c : variable range of z_c , discussed in the text.

^g $\Delta z_c / (z_c - z_s)$

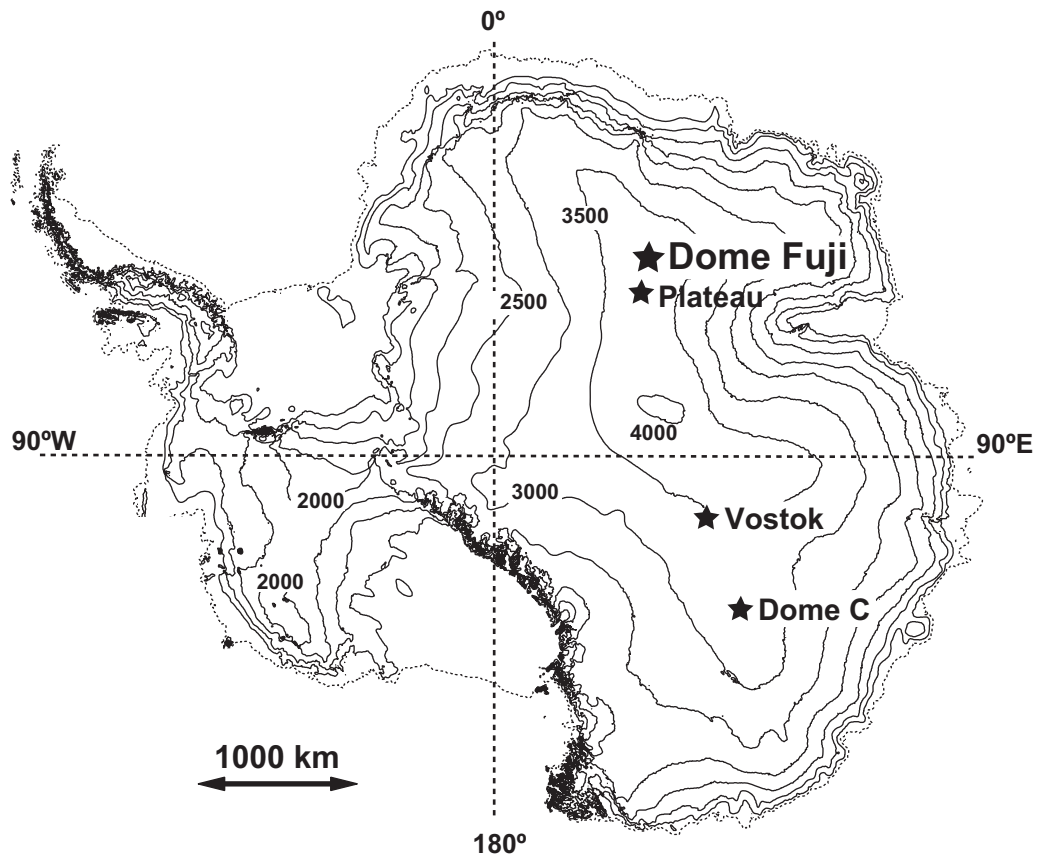


Figure 1

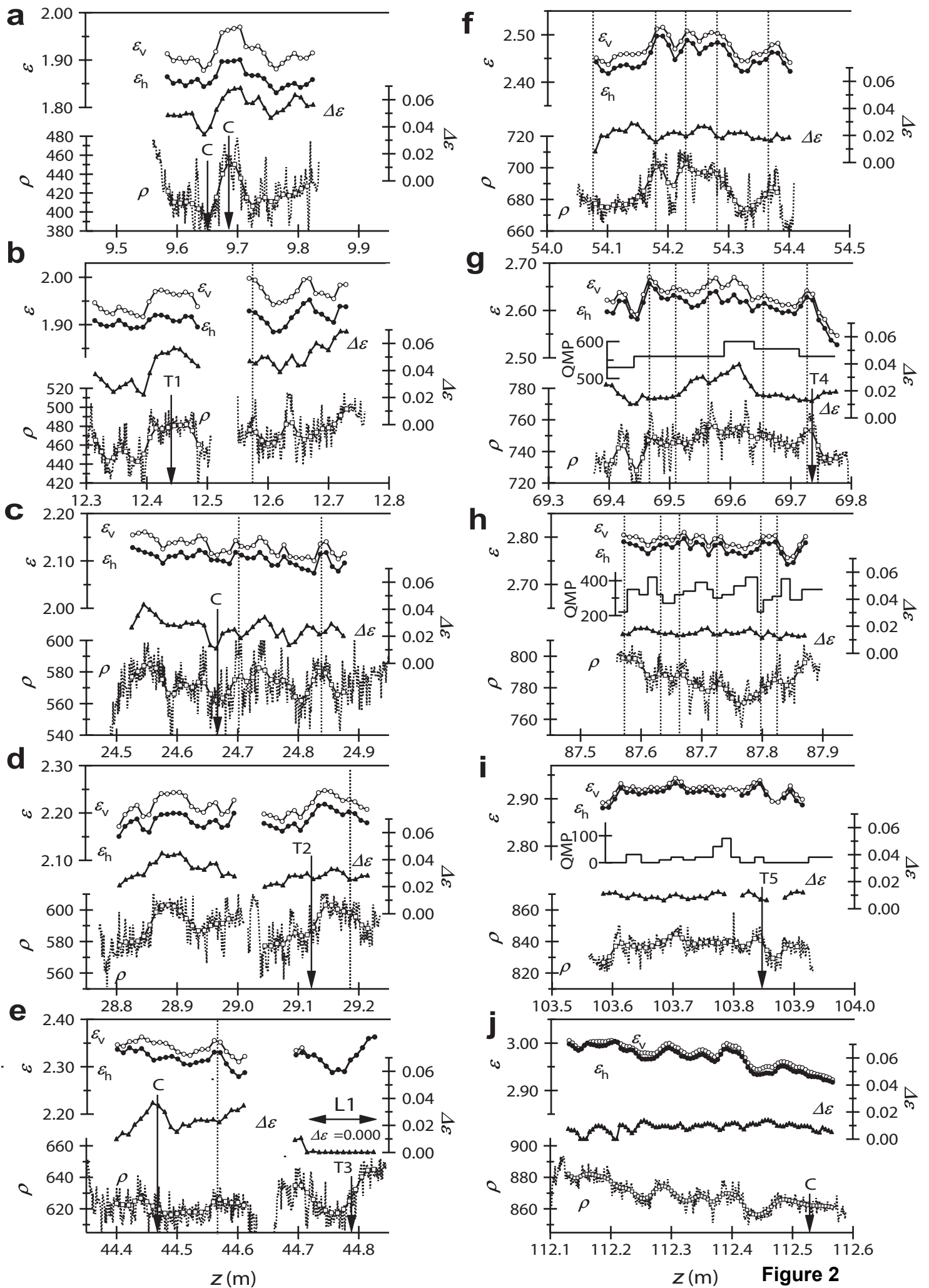


Figure 2

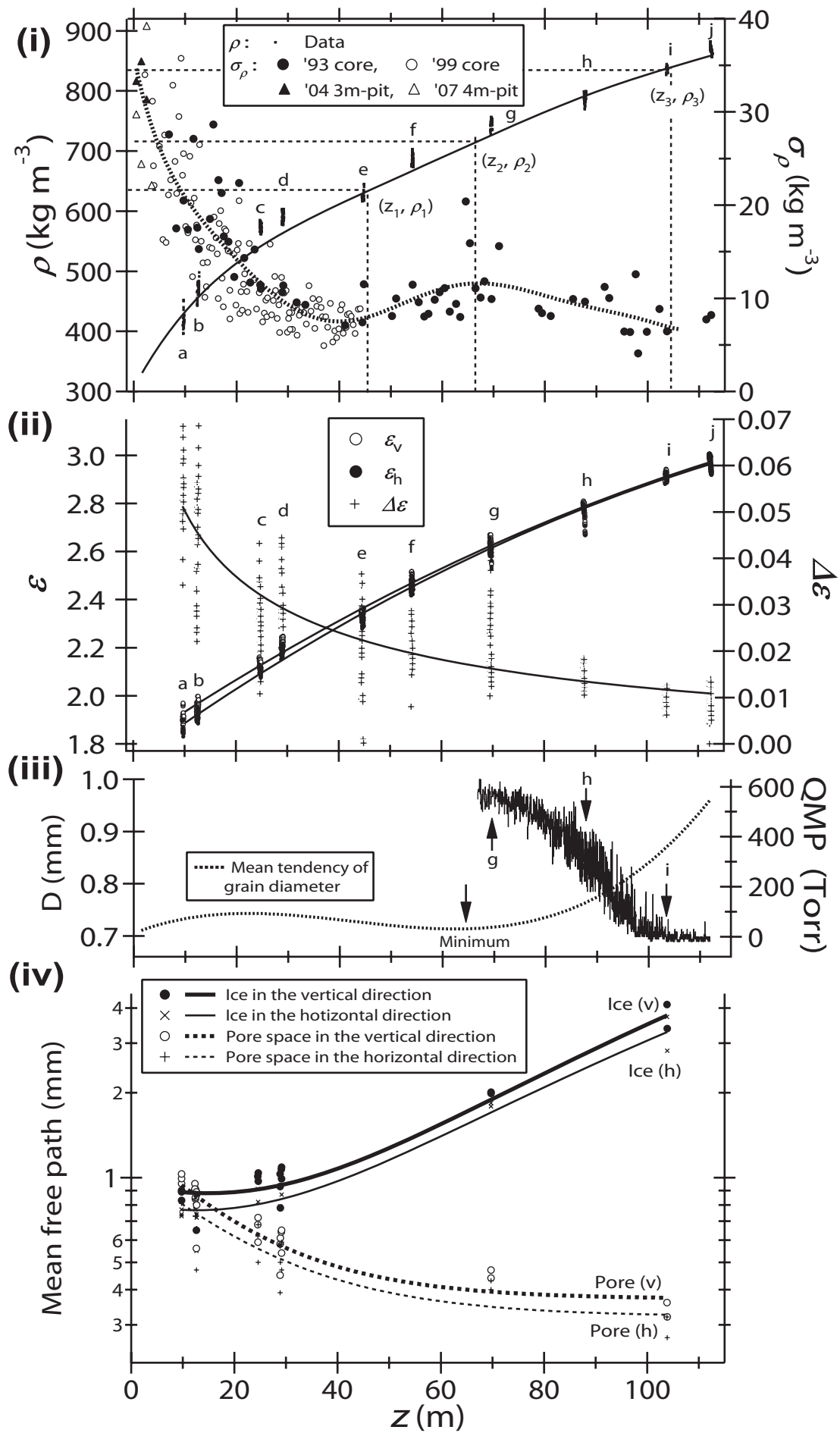


Figure 3

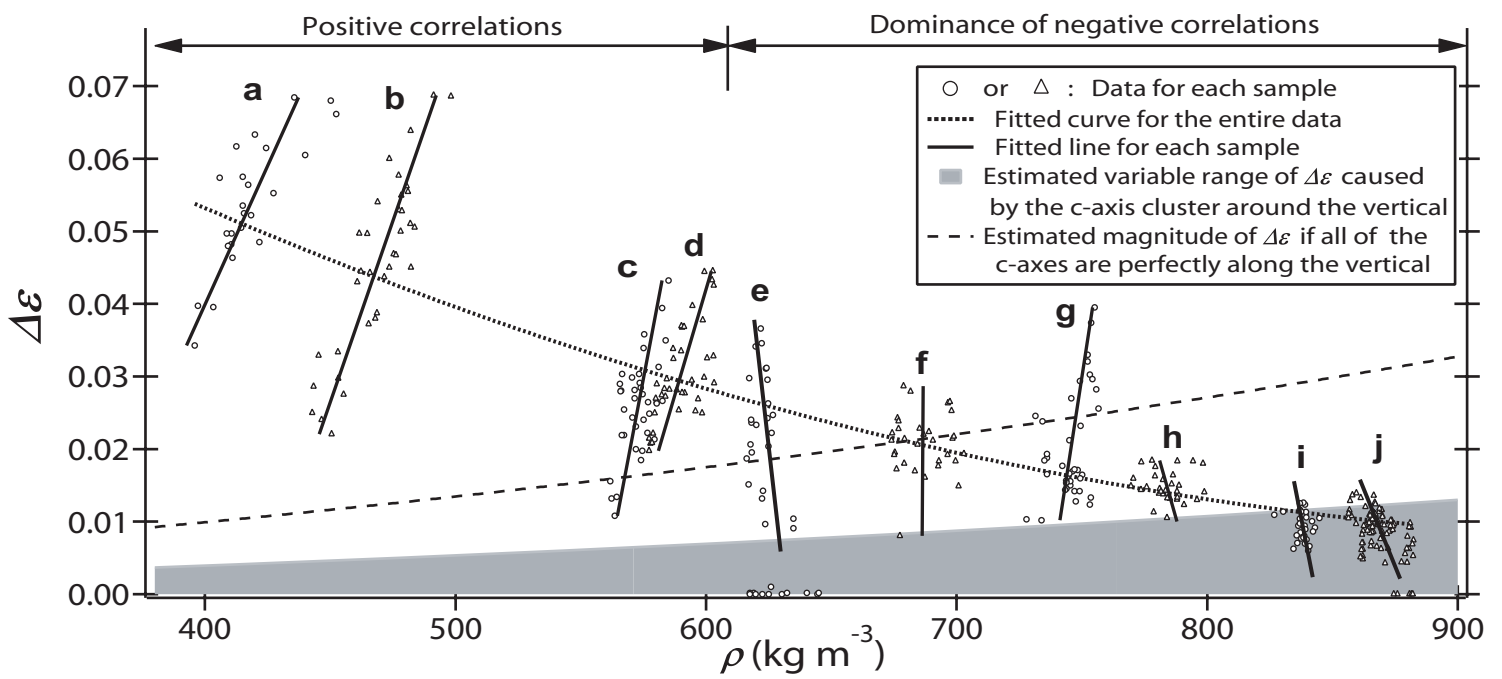


Figure 4

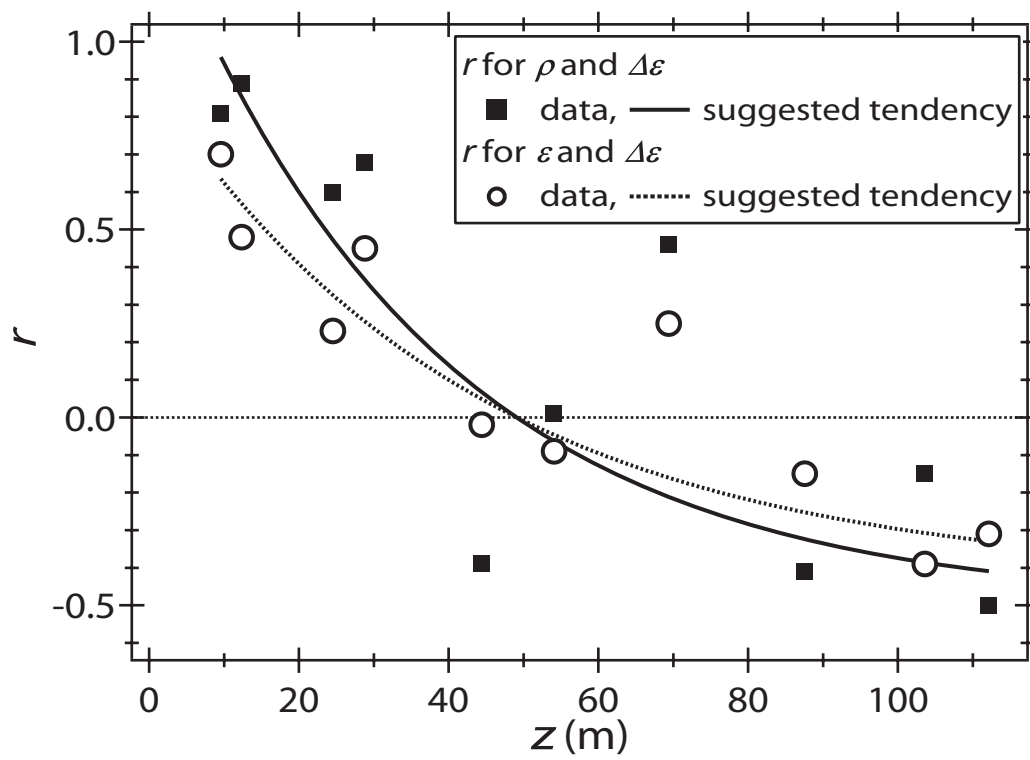


Figure 5

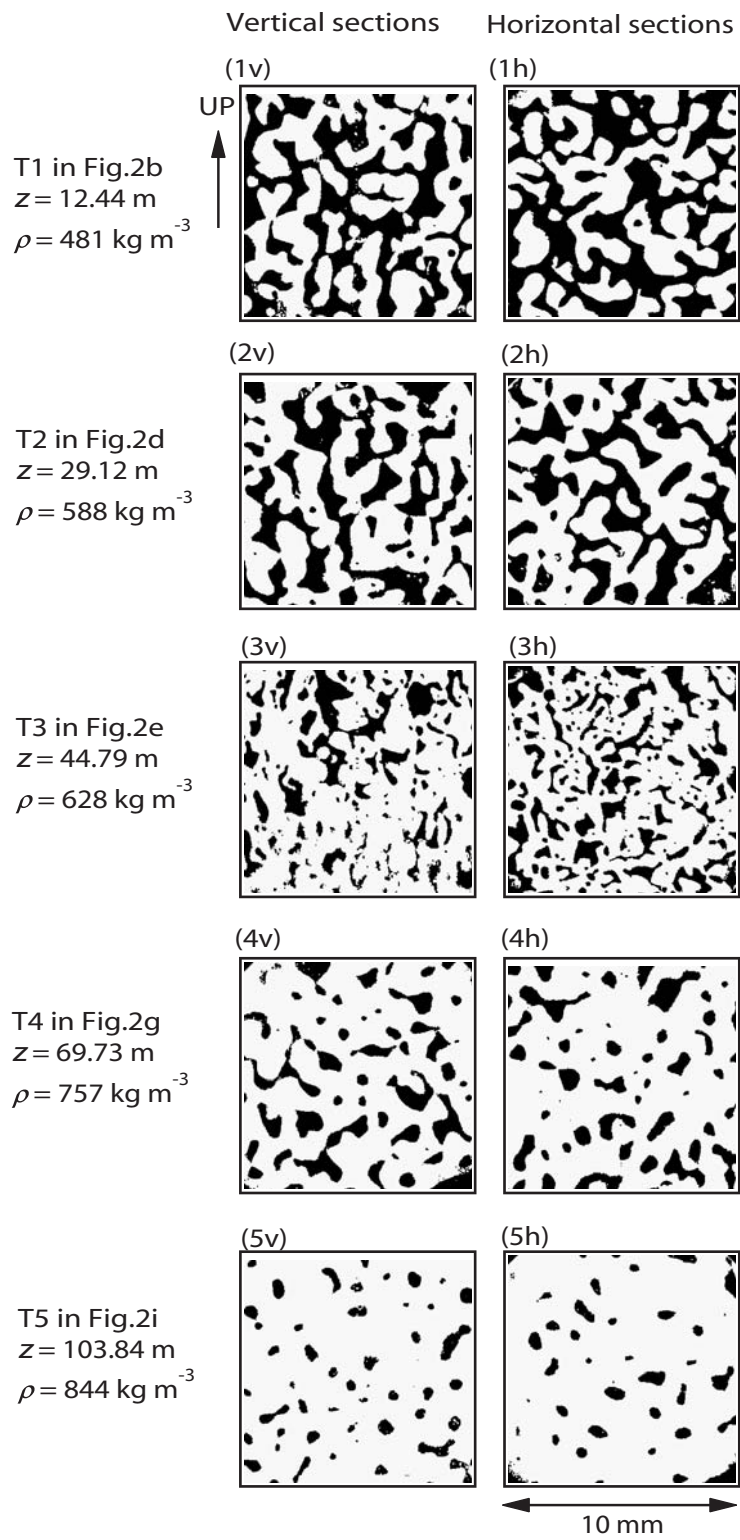


Figure 6

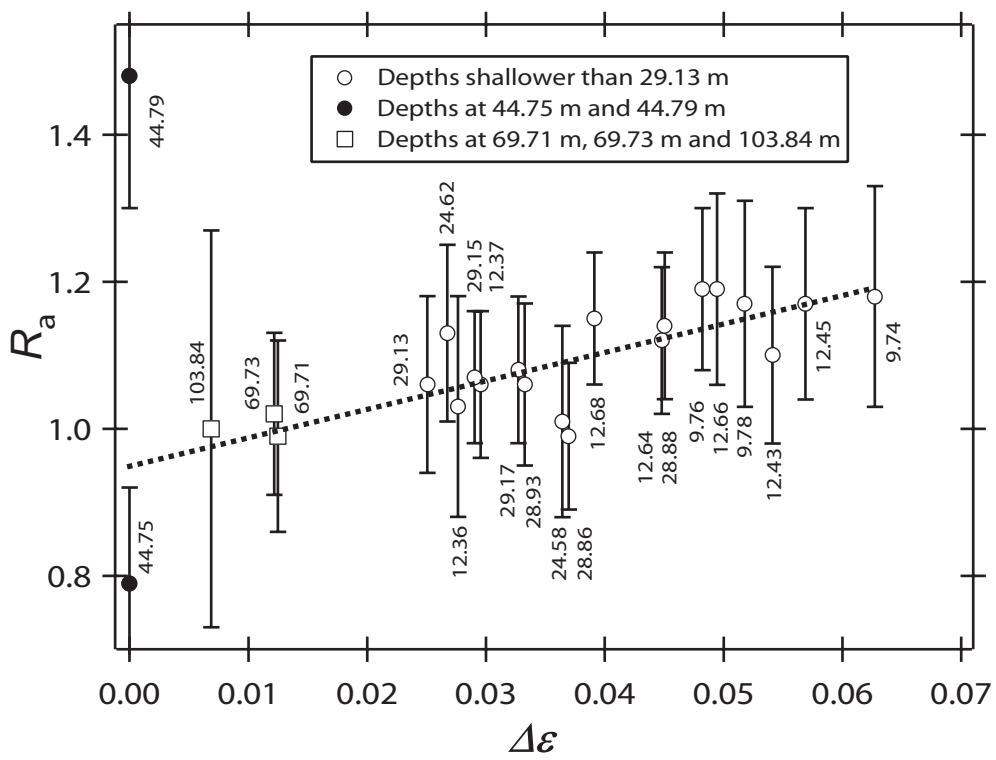


Figure 7

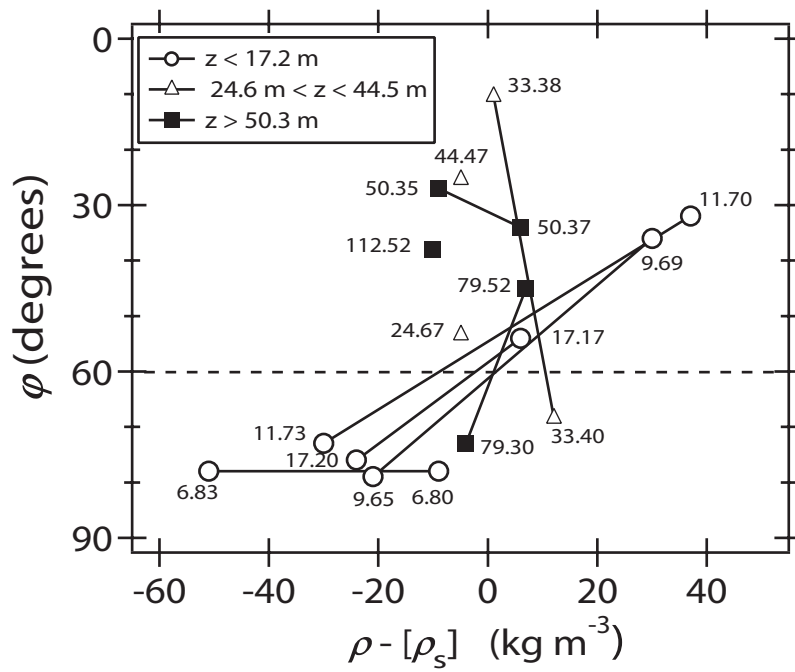


Figure 8

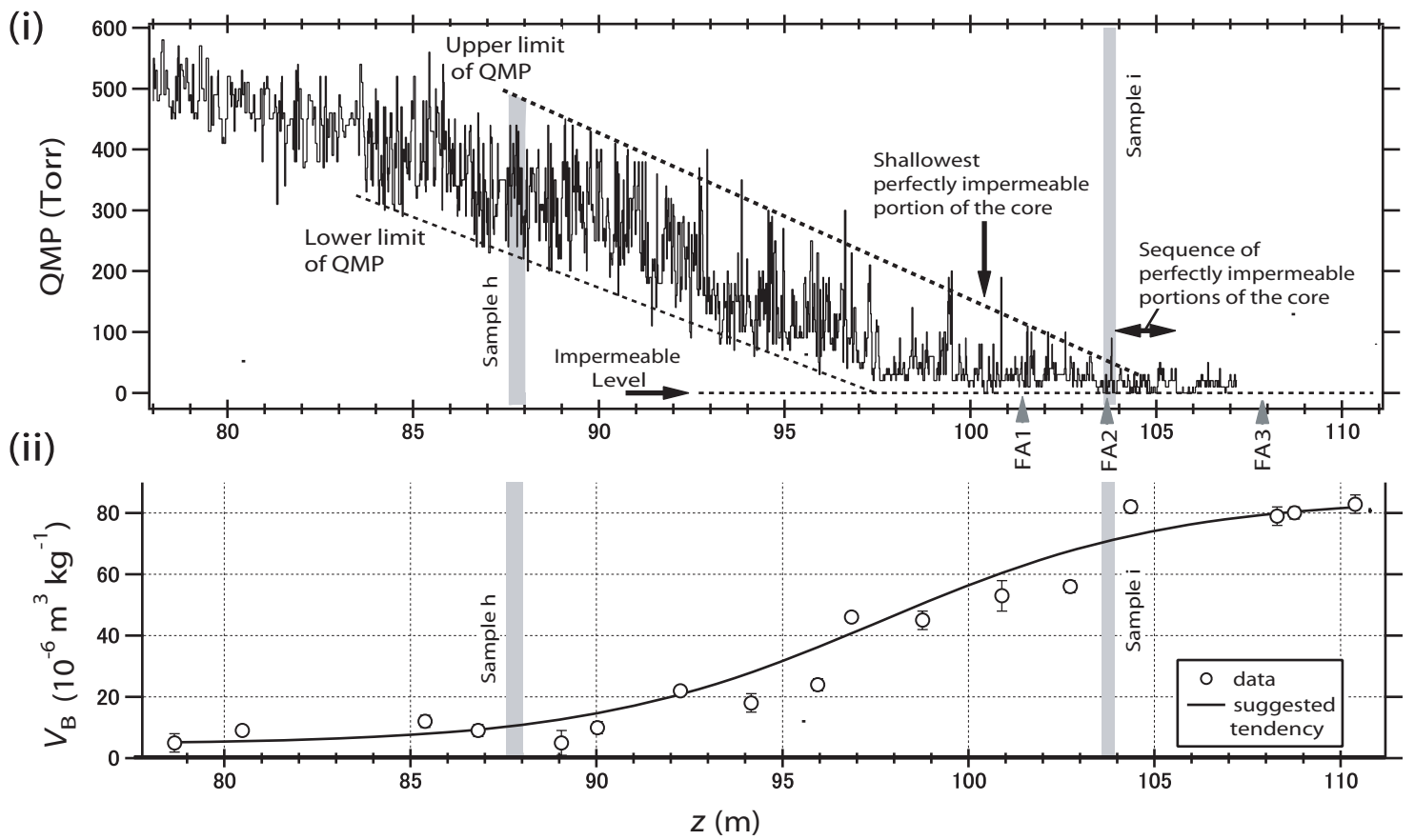


Figure 9

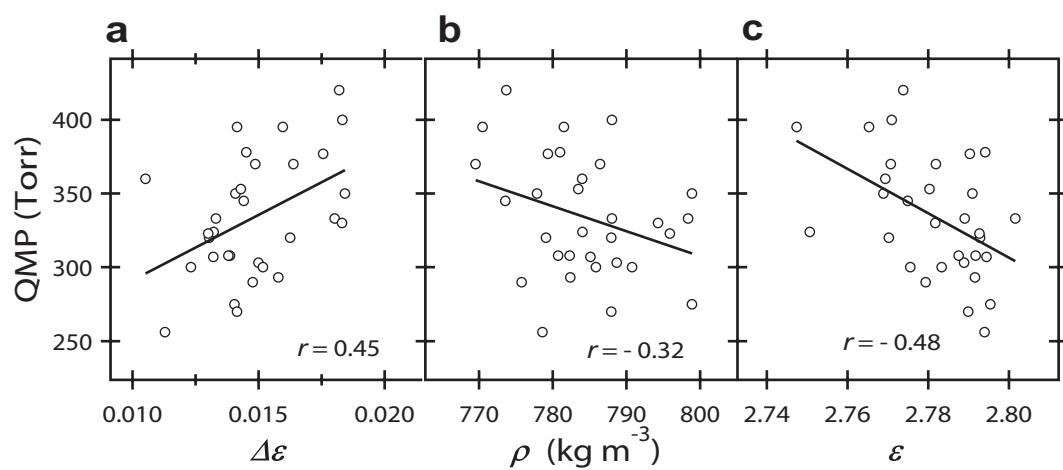


Figure 10

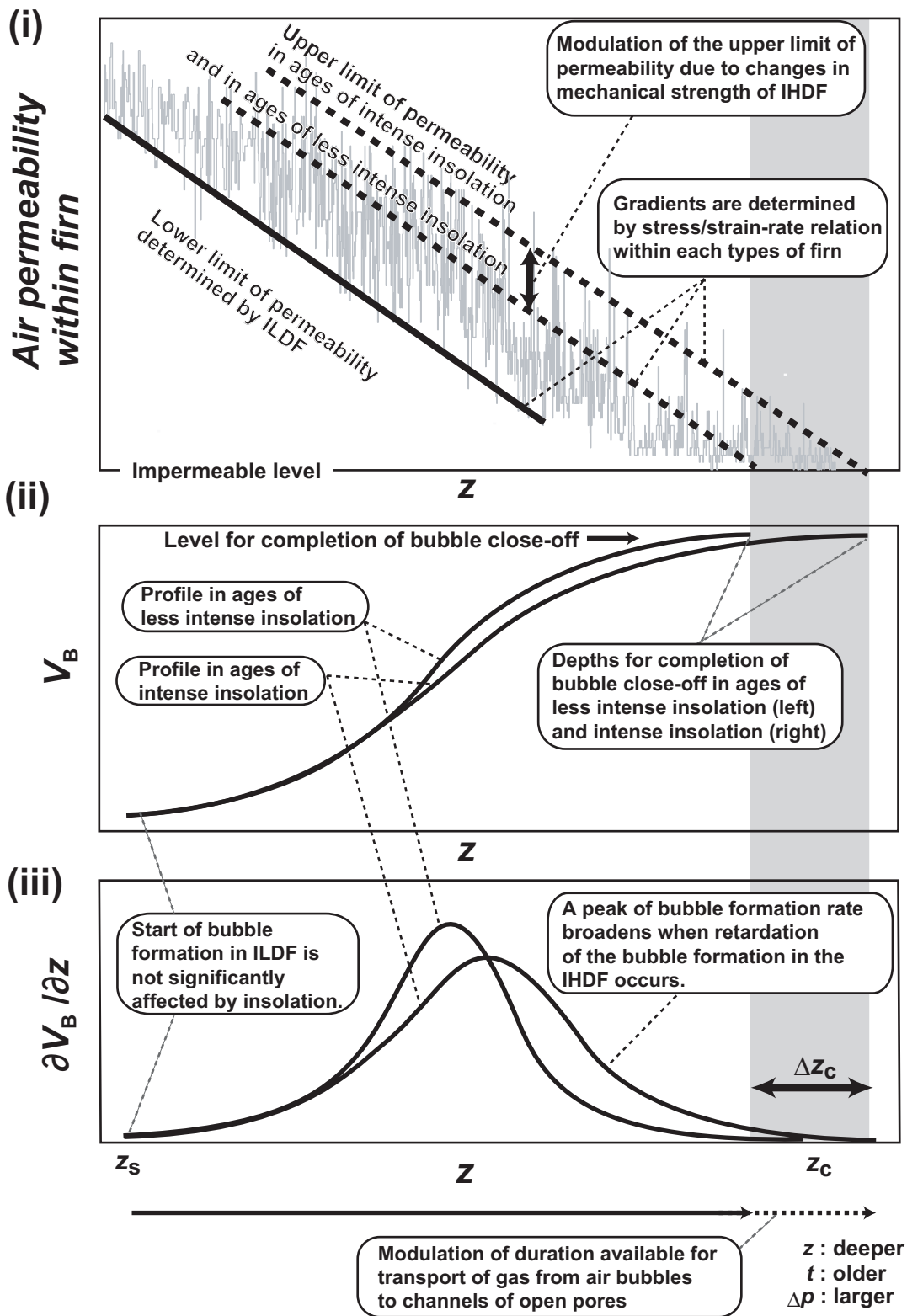


Figure 11